TADF material design – Photophysical background and case studies focusing on Cu(I) and Ag(I) complexes

Hartmut Yersin[†,*], Rafal Czerwieniec[†], Marsel Z. Shafikov[†,‡], Alfiya F. Suleymanova[†,§]

[†] University of Regensburg, Institute of Physical Chemistry, Universitätsstr. 31, D-93053 Regensburg, Germany.

[‡] Ural Federal University, Mira 19, Ekaterinburg, 620002, Russia.

[§] I. Postovsky Institute of Organic Synthesis, Ekaterinburg, 620990, Russia.

ChemPhysChem 2017, 18, 3508.
DOI: 10.1002/cphc.201700872

This work was supported in the framework of Marie Skłodowska-Curie Research and Innovation Staff Exchange (RISE) program

Project Number: 645628
Project Acronym: METCOPH

Project title: Metallocomplexes of macrocyclic compounds for photonic devices

TADF material design - Photophysical background and case studies focusing on Cu(I) and Ag(I) complexes

Hartmut Yersin[†,*], Rafal Czerwieniec[†], Marsel Z. Shafikov[†,‡], Alfiya F. Suleymanova[†,§]

[†] University of Regensburg, Institute of Physical Chemistry, Universitätsstr. 31, D-93053 Regensburg, Germany.

[‡] Ural Federal University, Mira 19, Ekaterinburg, 620002, Russia.

[§] I. Postovsky Institute of Organic Synthesis, Ekaterinburg, 620990, Russia.

* Corresponding author: hartmut.yersin@ur.de

Abstract

The development of organic light emitting diodes (OLEDs) and the use of emitting molecules have strongly stimulated scientific research of emitting compounds. In particular, for OLEDs it is required to harvest all singlet and triplet excitons that are generated in the emission layer. This can be achieved using the so-called *triplet harvesting mechanism.* However, the materials to be applied are based on high-cost rare metals and therefore, it has been proposed already more than one decade ago by our group to use the effect of thermally activated delayed fluorescence (TADF) to harvest all generated excitons in the lowest excited singlet state S_1. In this situation, the resulting emission is an $S_1 \rightarrow S_0$ fluorescence, though a delayed one. Hence, this mechanism represents the *singlet harvesting mechanism.* Using this effect, high-cost and strong SOC-carrying rare metals are not required. This mechanism can very effectively be realized by use of Cu(I) or Ag(I) complexes and even by purely organic molecules. In this investigation, we focus on photoluminescence properties and on crucial requirements for designing Cu(I) and Ag(I) materials that exhibit short TADF decay times at high emission quantum yields. The decay should be as short as possible

to minimize non-radiative quenching and, in particular, chemical reactions that frequently occur in the excited state. Thus, short TADF decay time can strongly increase the material's long-term stability. Here, we study crucial parameters and analyze their impact on the TADF decay time. For example, the energy separation $\Delta E(S_1{-}T_1)$ between the lowest excited singlet state S_1 and triplet state T_1 should be small. Accordingly, we present detailed photophysical properties of two case-study materials designed to exhibit a large $\Delta E(S_1\text{-}T_1)$ value of 1000 cm^{-1} (120 meV) and, for comparison, a small one of 370 cm^{-1} (46 meV). From these studies - extended by investigations of many other Cu(I) TADF compounds - we can conclude that just small $\Delta E(S_1\text{-}T_1)$ is not a sufficient requirement for short TADF decay time. High allowedness of the transition between the emitting S_1 state and the electronic ground state S_0, expressed by the radiative rate $k^r(S_1{\rightarrow}S_0)$ or the oscillator strength $f(S_1{\rightarrow}S_0)$, is also very important. However, mostly small $\Delta E(S_1\text{-}T_1)$ is related to small $k^r(S_1{\rightarrow}S_0)$. As a consequence, a reduction of τ(TADF) to below a few µs might be problematic. This relation results from an experimental investigation of a large number of Cu(I) complexes and basic quantum mechanical considerations. However, new materials can be designed for which this disadvantage is not prevailing. A new TADF compound, Ag(dbp)(P_2-nCB) (with dbp = 2,9-di-*n*-butyl-1,10-phenanthroline and P_2-nCB = *bis*-(diphenylphosphine)-*nido*-carborane) seems to represent such an example. Accordingly, this material shows TADF record properties, such as short TADF decay time at high emission quantum yield. These properties are based (i) on geometry optimizations of the Ag(I) complex for a fast radiative $S_1{\rightarrow}S_0$ rate and (ii) on restricting the extent of geometry reorganizations after excitation for reducing non-radiative relaxation and emission quenching. Indeed, we could design a TADF material with breakthrough properties showing τ(TADF) = 1.4 µs at 100 % emission quantum yield.

1. Introduction

Basic research of photophysical and chemical properties of organo-transition-metal compounds was strongly activated by their potential commercial use. This became particularly apparent for classes of compounds that may be applied as emitters in OLEDs[1-19] or in light emitting electrochemical cells (LEEC)[7,20-28]. These scientific investigations led to a much deeper understanding of photophysical principles and of the compound´s properties resulting in the development of an enormous number of new materials in part with drastically improved properties for OLED applications.[4,9,29-52] Improvements were also stimulated in the fields of related functional materials based on metal complexes for sensing of oxygen or temperature [53-59] or for photocatalysis [60-66].

For luminescent materials to be applied in OLEDs, it is essential that all excitons generated in the emission layer are harvested and converted into photons. Since the statistic ratio of the formed excitons is 1 singlet to 3 triplets [67-68], special mechanisms that allow to harvest all of them are required, as the two types of excitons show different relaxation properties. [67] Already about twenty years ago, it was discovered that third row transition metal complexes, especially those with Ir(III), Pt(II), or Os(II) metal centers are well suited for such harvesting processes, since the metal centers can induce efficient spin-orbit coupling (SOC)[69-77] between the lowest triplet state T_1 and higher lying singlet states S_n (with $n > 1$).[1,9,11-12,67,69-89] As a consequence, fast intersystem crossing (ISC) to the lowest triplet state of several tens of fs [88,90] can occur and relatively high radiative phosphorescent rates from the T_1 state to the electronic ground state S_0 are induced. These latter rates can become as high as $\approx 10^6\ s^{-1}$.[70,89,91] Therefore, these phosphorescent compounds are frequently denoted as triplet emitters. As a consequence, when applied in OLEDs, these materials can harvest all singlet and triplet excitons in the lowest excited triplet state. Accordingly, the corresponding mechanism is denoted as *triplet harvesting effect*. [69,78] Indeed, using for example

$Ir(ppy)_3$ (with ppy = 2-phenylpyridinate), OLEDs with almost 100 % internal quantum efficiency could be produced. [11,81]

However, these triplet emitter complexes require high-cost rare metals and this may become a limiting factor, when OLED lighting goes into mass production.[70,92-93] Therefore, an alternative harvesting mechanism that may work with low-cost materials has been proposed more than one decade ago.[94] This mechanism is based on the molecular effect of thermally activated delayed fluorescence (TADF) according to which also all excitons generated in the emission layer may be harvested. In this situation, however, the emission does not stem from the lowest excited triplet state, but from the thermally activated singlet state S_1. Hence, this mechanism has been denoted as *singlet harvesting mechanism*.[9,30-31,37,40,56,70,92,94-97] Accordingly, the luminescent materials do not need to contain high SOC-inducing metal centers (high cost materials), since the (thermally activated) singlet state usually carries sufficient allowedness with respect to the transition to the singlet ground state (spin-allowed transition). Therefore, an efficient path for photon generation becomes available.

Obviously, thermal activation, from the lowest triplet state T_1 to the higher lying singlet state S_1 requires a relatively small energy separation $\Delta E(S_1\text{-}T_1)$ between these states. For example, at ambient temperature (T = 300 K), a thermal energy of $k_BT \approx 210$ cm^{-1} (26 meV) is available (k_B = Boltzmann constant). Hence, as a rule of thumb, efficient thermal activation with fast up-ISC or reverse ISC (= RISC) is not expected to occur for $\Delta E(S_1\text{-}T_1)$ distinctly above 10^3 cm^{-1} (≈ 130 meV). Indeed, such energy separations can be realized with environmentally friendly and low-cost Cu(I) [4,9,27,30-35,37-56,70,92-93,95-105] and Ag(I)[104,106-109] complexes as well as with purely organic molecules. [110-114]

In this review, we focus on Cu(I) and Ag(I) complexes. For these materials, we have to address three crucial photophysical requirements:

(i) The emitter compounds should exhibit high photoluminescence quantum yields Φ_{PL}. After an electronic excitation, however, Cu(I) and Ag(I) complexes experience distinct flattening distortions with respect to the ground state geometries.[115-124] Usually, such geometry changes are related to an increase of non-radiative deactivation or even result in total quenching of the luminescence by vibrational relaxation. This is induced by a strong increase of the Franck-Condon factors of the low-lying vibrational modes of the excited electronic state and highly excited vibrational modes of the electronic ground state.[125-127] However, these shortcomings may be suppressed to a large extent by rigidifying the molecular structure either by sterically demanding ligands or by a rigid environment. This behavior has already been discussed frequently in the literature.[9,30-31,35,92,95-96,108-109,115,120,128] We will address these properties in sections 3 and 6. Interestingly, design of a material, a silver complex, with Φ_{PL} of 100 % becomes possible by following this strategy of rigidifying the molecular structure (See refs. [108-109] and section 6).

(ii) Well designed TADF materials should exhibit relatively small energy separations $\Delta E(S_1\text{-}T_1)$. For organo-transition metal compounds this is related to the occurrence of metal-to-ligand charge transfer (MLCT) (and ligand-to-ligand charge transfer (LL'CT)) states having frontier orbitals, HOMO and LUMO, that are spatially largely separated. This leads to a small exchange interaction[129-131] between the involved electrons and hence, to the required small splitting between the singlet S_1 and triplet T_1 state. In particular, a relatively small $\Delta E(S_1\text{-}T_1)$ value is a necessary condition to obtain a short radiative TADF decay time, which is important to maximize the photoluminescence quantum yield Φ_{PL}. Moreover, for use in OLEDs short decay times are important to minimize roll-off effects (for example, induced by saturation or triplet-polaron quenching) and to reduce device stability problems as well as undesired energy

transfer processes from the emitter dopant to the host. In sections 3 and 4, discussing case studies, we will present Cu(I) compounds and the dependence of photophysical properties on the $\Delta E(S_1\text{-}T_1)$ gap.

(iii) The TADF properties crucially depend on the allowedness of the $S_1 \rightarrow S_0$ fluorescence that is thermally activated from the lower lying triplet state. The reason is that the corresponding radiative rate $k^r(S_1 \rightarrow S_0)$ also governs the TADF decay time. $k^r(S_1 \rightarrow S_0)$ should be as large as possible to obtain a short TADF decay time. However, basic quantum chemical considerations show that this rate $k^r(S_1 \rightarrow S_0)$ and $\Delta E(S_1\text{-}T_1)$ correlate. We address this behavior in section 5.

Thus, designing of TADF compounds with short TADF decay time and high emission quantum yield is a challenge. For example, radiative TADF decay times of Cu(I) complexes of less than 3 - 5 µs have not been reported so far. [30-31,96] We will discuss this challenge in several sections of this investigation. In particular, in section 6, where we focus on designing new Ag(I) complexes, we will show how to develop a breakthrough TADF material [108-109] with a radiative TADF decay time of only 1.4 µs (at Φ_{PL} = 100 %) that is significantly shorter than so far reported.

This chapter is organized as follows: In section 2, we introduce different parameters that have to be addressed for designing efficient TADF materials based on Cu(I) and Ag(I) complexes and we present the materials studied in this chapter together with selected photophysical data. Sections 3 and 4 display case studies of Cu(I) complexes with large and small $\Delta E(S_1\text{-}T_1)$ energy separation, respectively. Furthermore, we discuss effects of SOC with respect to properties of the lowest triplet state, such as phosphorescence allowedness and zero-field splitting. In section 5, we show on a very simple quantum mechanical basis that the size of the energy gap $\Delta E(S_1\text{-}T_1)$ and the allowedness of the singlet S_1 → singlet S_0 transition are correlated. This result is clearly

supported by experimental data. In section 6, we present photophysical properties of a new TADF class of Ag(I) complexes and we show, how an extraordinarily efficient TADF material can be designed. Finally, in a conclusion, we will give a short summary and point to future perspectives.

2. TADF, molecular parameters, and diversity of materials

The molecular TADF effect was already reported more than five decades ago.[132-133] It can be described by use of Figure 1. By an optical excitation, one usually excites a singlet state, for example, higher lying vibrational levels of the S_1 state. Subsequently, fast vibrational relaxation of the order of 10^{-12} s [125] proceeds to lower lying vibrational levels. Then, depending on the class of molecules, prompt fluorescence and/or down-ISC (as well as non-radiative relaxation to the electronic ground state) can occur. For Cu(I) and Ag(I) complexes, being in the focus of this contribution, ISC from S_1 to the T_1 state is very effective, since fast intersystem crossing occurring in the time range of 3 to 30 ps has been observed. [119,122-123,134-135] The individual value depends on molecular properties, for example, on the extent of SOC of higher lying singlets to the lowest triplet state, but also on the local environment, such as a fluid or a rigid matrix.[135] In general, a significant prompt fluorescence ($S_1 \rightarrow S_0$) is not detected, but a very bright long-lived phosphorescence ($T_1 \rightarrow S_0$) is frequently observed at low temperature.[30-31,33-35,70,92,95-97,136-137] At higher temperature and in a situation of a fast thermal equilibration, population of the higher lying singlet state is governed by the Boltzmann distribution. As a consequence, the emission decays with a single decay time being a weighted average (eq. 1) of the $T_1 \rightarrow S_0$ and the thermally activated $S_1 \rightarrow S_0$ decay processes. Usually, this is observed for Cu(I) and Ag(I) complexes with low-lying MLCT states. At lower temperatures population of the S_1 state due to the Boltzmann thermal distribution is frozen out. To summarize, the weak prompt fluorescence decay component cannot

be detected at ns to µs time scales as used in our experiments. Thus, only the thermalized and equilibrated emission is observed that shows mono-exponential decay kinetics.

Additionally, it is mentioned that below T ≈ 15 K, effects of spin-lattice relaxation (SLR) between the triplet substates might strongly slow down relaxation processes. [31,33-34,88,95,138-140] Consequently, frequently a multi-exponential decay (from the different T_1 substates to the ground state S_0) is observed at very low temperature.

At higher temperatures, up-ISC processes efficiently depopulate the triplet T_1 state, i.e. the three triplet substates, and populate the singlet S_1 state. In particular, if the emission decay time of the T_1 state is long, for example longer than several 100 µs, the phosphorescence is largely "quenched" and almost only the $S_1 \rightarrow S_0$ fluorescence is observed. Because the population of the S_1 state is fed from the long-living triplet state (triplet reservoir), this type of fluorescence is also long-living compared to the prompt fluorescence that does not involve a triplet state. Hence, the emission is denoted as thermally activated *delayed* fluorescence.

For completeness, it is mentioned that for several Cu(I) complexes, SOC with respect to the T_1 state is significant. In this situation, the TADF process will not fully deplete the T_1 state during its much shorter population time and a combined TADF/phosphorescence is observed. This property is not in the focus of the present contribution, but is discussed in detail in the literature.[31,33-34,97]

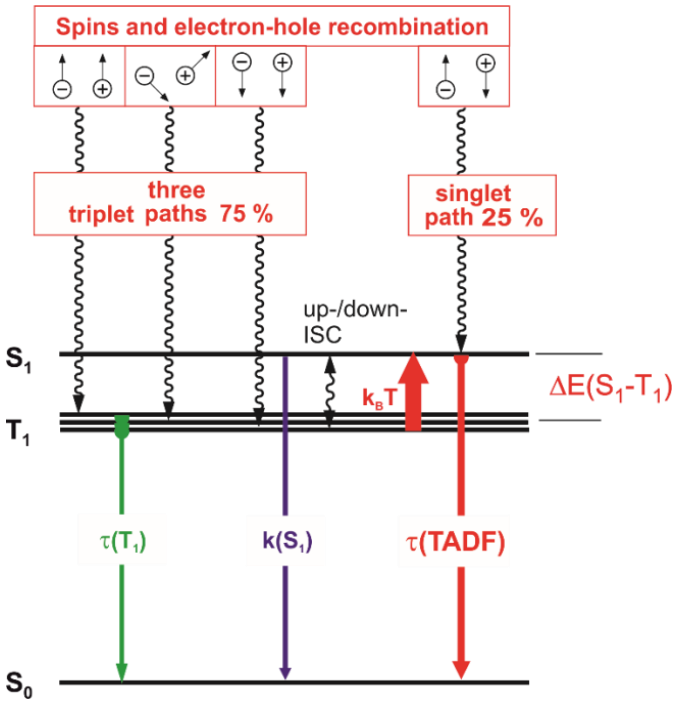

Figure 1. Illustration of the molecular TADF effect and its use in OLEDs (singlet harvesting). $\tau(T_1)$ and τ(TADF) are the phosphorescence decay time and the TADF decay time, respectively. $k(S_1) = k^r(S_1 \rightarrow S_0)$ is the radiative rate of the $S_1 \rightarrow S_0$ transition (prompt fluorescence). Up-ISC is also often denoted as reverse intersystem crossing (RISC).

In the emission layer of an OLED device, the electron-hole recombination produces excitons of different spin-multiplicity, that is 75 % are of triplet and 25 % of singlet character. [67-68,78-79] (Figure 1) These excitons can be trapped in the emitter molecule. Such mechanisms are discussed in ref.[67]. Subsequently, fast internal conversions, i.e. one singlet path and three triplet paths, populate the S_1 and the T_1 state, respectively.[67] Then similarly to the behavior after optical excitation, thermal activation takes place. In particular, in a situation of a forbidden $T_1 \rightarrow S_0$ transition and a relatively small $\Delta E(S_1\text{-}T_1)$ value finally almost all excitations are transferred to the lowest excited singlet state, which then exhibits a delayed $S_1 \rightarrow S_0$ fluorescence. According to this process, the molecular TADF effect as exploited in an OLED device has been denoted as *singlet harvesting mechanism*.[9,30-31,70,94-96]

As already stressed, the TADF decay time τ(TADF) should be as short as possible (obviously, at a high emission quantum yield), if the emitter is applied in an OLED. To achieve this goal, valuable guidelines can be deduced. Especially, a discussion of the temperature dependence of the emission decay time is helpful. This is easily explained by use of a model discussion of a simplified molecule with two excited states, a singlet S_1 and a triplet T_1, being in fast thermal equilibrium, and the electronic ground state S_0. (Compare Figure 1) In this situation, the decay time $\tau(T)$ of the luminescent molecule is described by a Boltzmann-type relation[30] (compare also[141-144]):

$$\tau(\mathrm{T}) = \frac{3+\exp\left(-\frac{\Delta E(S_1-T_1)}{k_B T}\right)}{3k(T_1)+k(S_1)\exp\left(-\frac{\Delta E(S_1-T_1)}{k_B T}\right)} \qquad (1)$$

$k(T_1) = 1/\tau(T_1)$ and $k(S_1) = 1/\tau(S_1)$ are the decay rates with the decay times $\tau(T_1)$ and $\tau(S_1)$ of the triplet and singlet excited state, respectively, and $\Delta E(S_1\text{-}T_1)$ is the energy separation between the S_1 and T_1 state. $\tau(T)$ represents the experimentally accessible emission decay time at a given temperature. For the subsequent discussion, it is assumed that the molecular parameters $\tau(T_1)$, $\tau(S_1)$, and $\Delta E(S_1\text{-}T_1)$ are temperature independent and that the splitting of the triplet state into three substates (zero-field splitting, ZFS) is small, i.e. much smaller than k_BT.

For completeness, it is remarked that application of eq. (1) to the measured decay times at different temperatures opens access to the molecular parameters given above. In particular, it becomes possible to determine very small energy separations being much below the attainable spectral resolution. For example, using a slightly modified eq. (1) energy separations of only a few cm^{-1} can be resolved despite the fact that the MLCT emission bands are frequently as broad as several thousand cm^{-1}. (Compare [9,31,95,97,141].)

At very low temperature, the exponential terms in eq. (1) are negligible and the measured decay time $\tau(T)$ displays the phosphorescence decay time $\tau(T_1)$, while at high temperature (and long $\tau(T_1)$) the term containing $\tau(T_1)$ can be neglected and one obtains essentially the decay time $\tau(TADF)$. Below in sections 3, 4, and 6, several case studies, discussing the $\tau(T)$ temperature behavior, are presented.

Eq. (1) shows that three parameters crucially determine the emission decay time. These parameters can be deduced from fitting eq. (1) to the measured emission decay times for a suitable temperature range. If this is carried out for a number of Cu(I) and/or Ag(I) complexes, valuable guidelines for molecular design rules can be extracted. Therefore, a more detailed discussion of the three parameters is illustrative.

Figure 2 schematically visualizes the photophysical background of the parameters that govern eq. (1). For all three cases, subsequently discussed in detail, it is assumed that the respective molecule shows TADF.

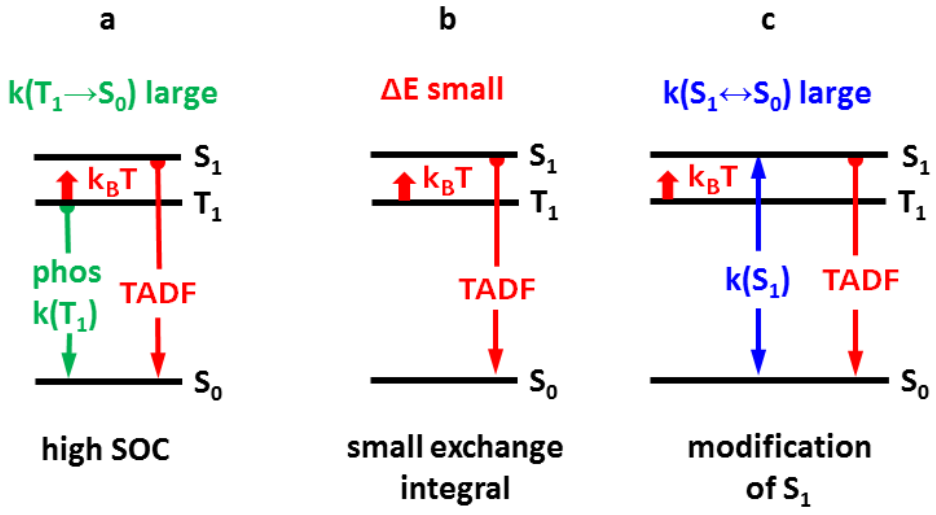

Figure 2. Different strategies for minimizing the emission decay time of TADF compounds for OLED applications. The zero-field splitting of the T_1 state into three sub-states is not shown in this diagram.

TADF and phosphorescence

Figure 2a displays an energy level diagram of a compound that exhibits significant SOC of the triplet state T_1 to a singlet state. Quantum mechanical considerations show that SOC between the triplet state T_1 and the singlet state S_1 both stemming from the same orbital configuration vanishes. [9,30-31,69-77] However, mixing-in of different, higher lying singlets S_n (with $n > 1$) can be significant. If so, the triplet state of Cu(I) complexes, for example, exhibits a distinct ZFS of several cm^{-1} (a few 0.1 meV) and the $T_1 \rightarrow S_0$ transition rate for the phosphorescence can become as large as $5 \cdot 10^4$ s^{-1} (20 μs).[30,34,97,136-137] Accordingly, a second, effective radiative decay channel is opened in addition to the TADF decay path. These combined radiative decay paths can distinctly shorten the ambient temperature emission decay time. In this contribution, we do not focus further on this effect, but compare the literature reports. [30,34,97,145]

Minimizing $\Delta E(S_1\text{-}T_1)$

As already addressed, the energy separation $\Delta E(S_1\text{-}T_1)$ between the lowest singlet S_1 and triplet state T_1 should be relatively small. (Figure 2b) This can be well achieved with Cu(I) and Ag(I) complexes, if the lowest lying excited states are largely of ^{1,3}MLCT character. In this situation, a distinct charge separation between the unpaired electrons can occur. As a consequence, the quantum mechanical exchange interaction [129-131] and hence, also the singlet-triplet splitting becomes small. (Section 5) Because $\Delta E(S_1\text{-}T_1)$ enters in an exponential term in eq. (1), $\Delta E(S_1\text{-}T_1)$ reduction has a dominating effect on the TADF decay time, τ(TADF). However, this seems to be limited, when $\Delta E(S_1\text{-}T_1)$ becomes lower than 200 to 300 cm^{-1} (25 to ≈ 40 meV), since at smaller splitting, decrease of the S_1–S_0 transition rate $k^r(S_1 \rightarrow S_0)$ might induce an opposite trend and lead to an increase of τ(TADF). (In section 5 it will be shown that $\Delta E(S_1\text{-}T_1)$ and

$k^r(S_1 \rightarrow S_0)$ are related to each other.) The variation of $\Delta E(S_1\text{-}T_1)$ can be achieved by a suitable molecular design as discussed below in this section and in the case studies presented in the next two sections.

Importance of $k^r(S_1 \rightarrow S_0)$

The allowedness of the $S_1 \leftrightarrow S_0$ transition can be expressed, for example, by the radiative fluorescence rate $k^r(S_1 \rightarrow S_0)$. (Figure 2c) According to eq. (1), this rate plays also an important role at determining the TADF decay time. Frequently, this property is not adequately addressed. The rate should be as high as possible to obtain short TADF decay time. For this requirement, also $\Delta E(S_1\text{-}T_1)$ should be as small as possible. However, the two photophysical parameters are correlated. Small splitting $\Delta E(S_1\text{-}T_1)$ requires a small exchange interaction between the unpaired electrons, at least when both T_1 and S_1 states are well described by a HOMO-LUMO excitation. For a small exchange interaction, small overlap of HOMO and LUMO is advantageous. At the same time, small HOMO-LUMO overlap leads to a small oscillator strength (small allowedness) of the $S_1 \rightarrow S_0$ transition, and thus, to a small $k^r(S_1 \rightarrow S_0)$ value and hence, to a long fluorescence decay time. Indeed, experimental studies on Cu(I) complexes exhibiting TADF reveal that such a correlation exists for a large number of compounds (compare also section 5).[31]

However, it is indicated that a close correlation between these two photophysical properties might not always be so strict. In particular, the S_1 state might be modified by a suitable molecular design. For example, quantum mechanical configuration interaction can be helpful in this respect. This means that a different, higher lying singlet state, which is energetically proximate and carries high allowedness (high oscillator strength) with respect to the transition to the electronic ground state, can mix with the

S_1 state and induce a higher $S_1 \rightarrow S_0$ allowedness. Presumably, this mechanism is important for the Ag(I) complexes discussed in section 6.

Experimental access to the photophysical parameters as discussed above and in Figure 2 becomes possible by use of a fitting procedure of eq. (1) to the measured values of $\tau(T)$ over a large temperature range. The required range depends on the size of $\Delta E(S_1\text{-}T_1)$. For example, if $\Delta E(S_1\text{-}T_1)$ values are larger than about 700 cm^{-1} (87 meV) a temperature range of 77 K ≤ T ≤ 300 K might usually be sufficient. However, for smaller splittings, the range has to be extended, for example, to T = 30 K to be able to characterize a compound with a splitting of only $\Delta E(S_1\text{-}T_1)$ = 370 cm^{-1} (compound **2**, see section 4) [31,96]. Moreover, if the splitting of the T_1 state into substates of a few cm^{-1} (a few 0.1 meV) and the corresponding photophysical properties should be addressed, extension of the temperature range to about T = 1.3 K (and application of a slightly modified eq. (1) is required [58,70,88-89,97,139,146].

In sections 3, 4, and 6, we will present case studies. In these we will show how to develop a deeper understanding of representative compounds. In Table 1, for a broader overview, we summarize a selection of photophysical data for a large number of complexes that are addressed in this contribution. The compounds studied were investigated as powder materials. In this respect, it should be remarked that very frequently, the decay behavior measured of powder materials is modified, for example, by processes of energy transfer or triplet-triplet annihilation. However, if the low-lying CT states of the complexes exhibit geometry distortions also in the relatively rigid crystalline environment, localization (self-trapping) can occur and prevent energy transfer effects. Thus, the emission of the powder material can display molecular properties. Accordingly, concentration quenching does not occur and the decay

behavior does not show any distinctive feature (such as shortening of decay times) with concentration increase.[30-31,58,95]

Table 1. Photophysical data based on luminescence measurements of powder materials arranged according to increasing $\Delta E(S_1\text{-}T_1)$. $\Delta E(S_1\text{-}T_1)$ and $\tau(S_1 \rightarrow S_0)$ values result from fitting procedures. A prompt fluorescence of the S_1 state has not been observed directly. (Compare also Ref. [31].)

Compound	Photophysical data	References
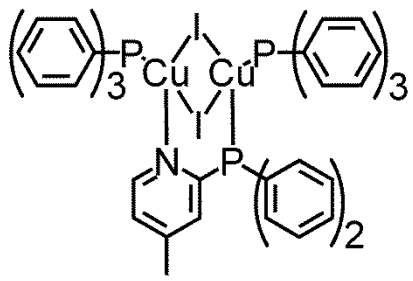 $Cu_2I_2(MePyrPhos)(Pph_2)_2$ **1**	**$\Delta E(S_1\text{-}T_1)$ = 270 cm^{-1}** λ_{max}(300 K) = 511 nm Φ_{PL}(300 K) = 97 % τ(300 K) = 5 µs $\tau(T_1 \rightarrow S_0)$ = 23 µs $\tau(S_1 \rightarrow S_0)$ = 570 ns	[31,38]
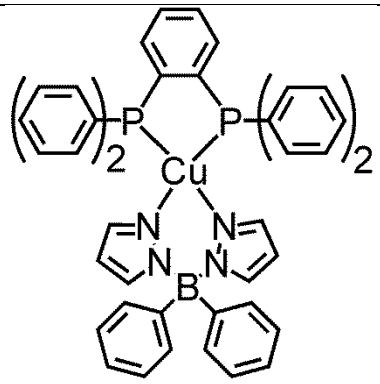 Cu(dppb)(pz_2Bph_2) **2**	**$\Delta E(S_1\text{-}T_1)$ = 370 cm^{-1}** λ_{max}(300 K) = 535 nm Φ_{PL}(300 K) = 70 % τ(300 K) = 3.3 µs $\tau(T_1 \rightarrow S_0)$ = 1200 µs $\tau(S_1 \rightarrow S_0)$ = 180 ns	[43,96,147]

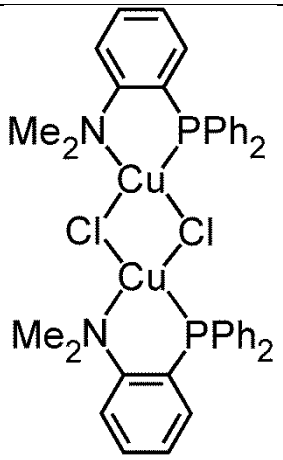 [Cu(μ-Cl)(PNMe2)]2 **3**	**$\Delta E(S_1\text{-}T_1) = 460\ cm^{-1}$** λ_{max}(300 K) = 506 nm Φ_{PL}(300 K) = 45 % τ(300 K) = 6.6 μs $\tau(T_1 \rightarrow S_0)$ = 250 μs $\tau(S_1 \rightarrow S_0)$ = 210 ns	[33]
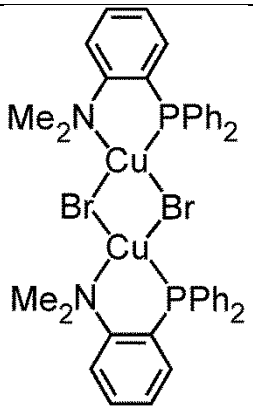 [Cu(μ-Br)(PNMe2)]2 **4**	**$\Delta E(S_1\text{-}T_1) = 510\ cm^{-1}$** λ_{max}(300 K) = 490 nm Φ_{PL}(300 K) = 65 % τ(300 K) = 4.1 μs $\tau(T_1 \rightarrow S_0)$ = 1200 μs $\tau(S_1 \rightarrow S_0)$ = 110 ns	[33]
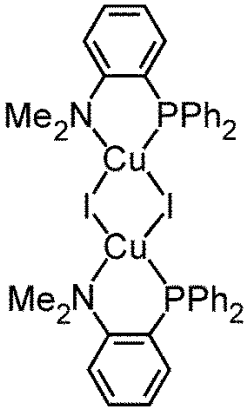 [Cu(μ-I)(PNMe2)]2 **5**	**$\Delta E(S_1\text{-}T_1) = 570\ cm^{-1}$** λ_{max}(300 K) = 464 nm Φ_{PL}(300 K) = 65 % τ(300 K) = 4.6 μs $\tau(T_1 \rightarrow S_0)$ = 290 μs $\tau(S_1 \rightarrow S_0)$ = 90 ns	[33]

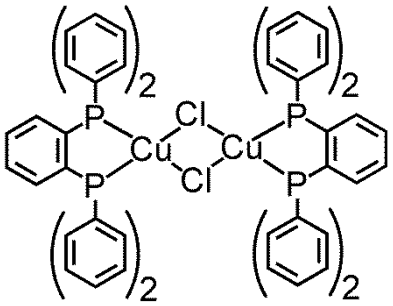 $Cu_2Cl_2(dppb)_2$ **6**	**$\Delta E(S_1\text{-}T_1)$ = 600 cm^{-1}** λ_{max}(300 K) = 545 nm Φ_{PL}(300 K) = 35 % τ(300 K) = 3 μs $\tau(T_1 \rightarrow S_0)$ = 2200 μs $\tau(S_1 \rightarrow S_0)$ = 70 ns	[100,107]
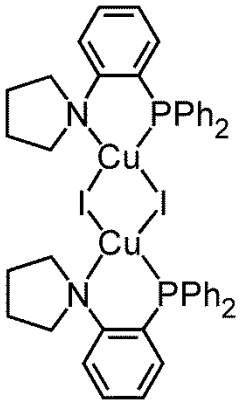 $[Cu(\mu\text{-}I)(PNpy)]_2$ **7**	**$\Delta E(S_1\text{-}T_1)$ = 630 cm^{-1}** λ_{max}(300 K) = 465 nm Φ_{PL}(300 K) = 65 % τ(300 K) = 5.6 μs $\tau(T_1 \rightarrow S_0)$ = 250 μs $\tau(S_1 \rightarrow S_0)$ = 100 ns	[33]
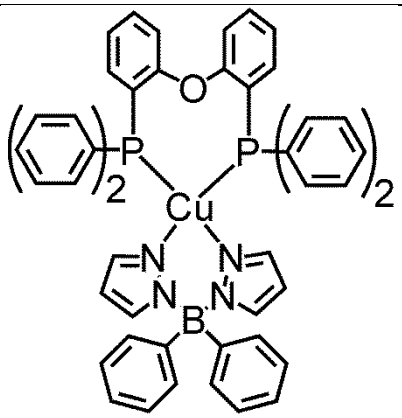 Cu(pop)(pz_2Bph_2) **8**	**$\Delta E(S_1\text{-}T_1)$ = 650 cm^{-1}** λ_{max}(300 K) = 464 nm Φ_{PL}(300 K) = 90 % τ(300 K) = 13 μs $\tau(T_1 \rightarrow S_0)$ = 500 μs $\tau(S_1 \rightarrow S_0)$ = 170 ns	[9,95,148-149]

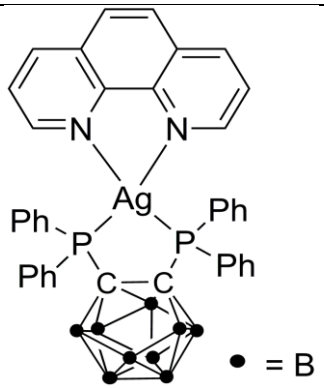 Ag(phen)(P_2-nCB) **9**	**$\Delta E(S_1\text{-}T_1)$** –[a] λ_{max}(300 K) = 575 nm Φ_{PL}(300 K) = 36 % τ(300 K) = 2 μs τ(77K) = 270 μs $\tau(S_1 \rightarrow S_0)$ –	[109] Table 7
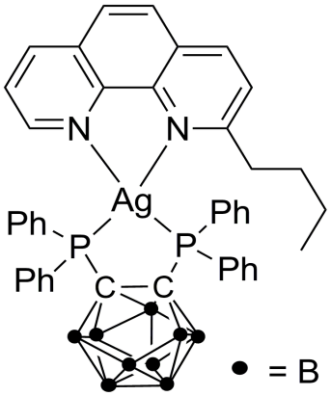 Ag(mbp)(P_2-nCB) **10**	**$\Delta E(S_1\text{-}T_1)$ = 640 cm^{-1}** λ_{max}(300 K) = 535 nm Φ_{PL}(300 K) = 70 % τ(300 K) = 2 μs $\tau(T_1 \rightarrow S_0)$ = 1600 μs $\tau(S_1 \rightarrow S_0)$ = 32 ns	[109] Table 7
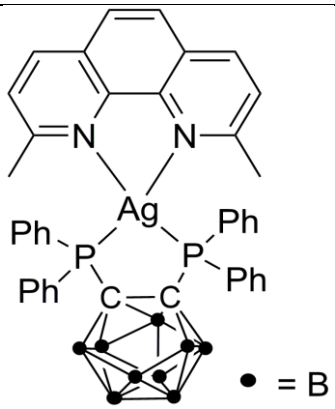 Ag(dmp)(P_2-nCB) **11**	**$\Delta E(S_1\text{-}T_1)$ = 650 cm^{-1}** λ_{max}(300 K) = 537 nm Φ_{PL}(300 K) = 78 % τ(300 K) = 2.8 μs $\tau(T_1 \rightarrow S_0)$ = 890 μs $\tau(S_1 \rightarrow S_0)$ = 36 ns	[109] Table 6

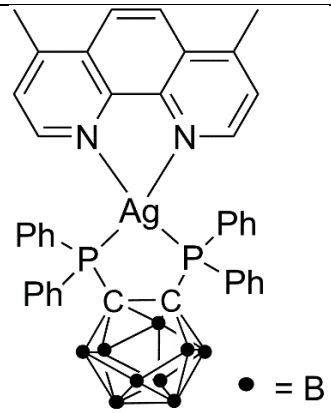 Ag(idmp)(P_2-nCB) **12**	**$\Delta E(S_1\text{-}T_1)$**[a] λ_{max}(300 K) = 562 nm Φ_{PL}(300 K) = 45 % τ(300 K) = 1.7 μs $\tau(T_1 \rightarrow S_0)$ = 475 μs	[109]
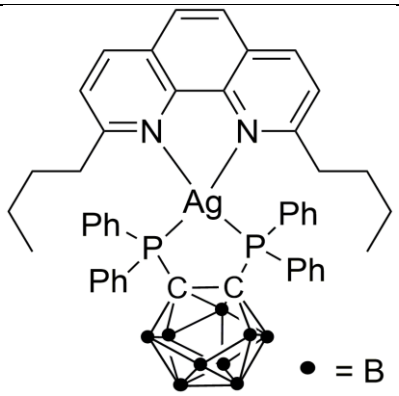 Ag(dbp)(P_2-nCB) **13**	**$\Delta E(S_1\text{-}T_1)$ = 650 cm^{-1}** λ_{max}(300 K) = 526 nm Φ_{PL}(300 K) = 100 % τ(300 K) = 1.4 μs $\tau(T_1 \rightarrow S_0)$ = 1570 μs $\tau(S_1 \rightarrow S_0)$ = 18 ns	[108-109]
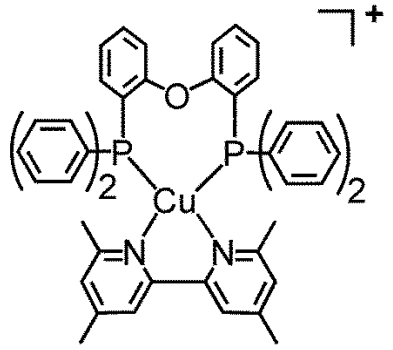 Cu(tmbpy)(pop)$^+$ **14**[b]	**$\Delta E(S_1\text{-}T_1)$ = 720 cm^{-1}** λ_{max}(300 K) = 555 nm Φ_{PL}(300 K) = 55 % τ(300 K) = 11 μs $\tau(T_1 \rightarrow S_0)$ = 84 μs $\tau(S_1 \rightarrow S_0)$ = 160 ns	[35]
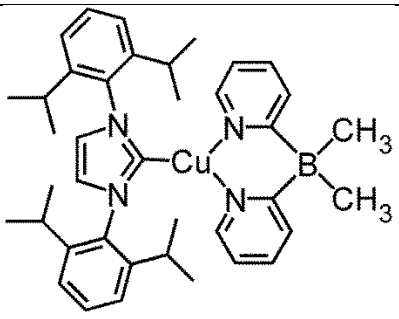 (IPr)Cu(py$_2$-BMe$_2$) **15**	**$\Delta E(S_1\text{-}T_1)$ = 740 cm^{-1}** λ_{max}(300 K) = 475 nm Φ_{PL}(300 K) = 76 % τ(300 K) = 11 μs $\tau(T_1 \rightarrow S_0)$ = 34 μs	[34,150]

	$\tau(S_1 \rightarrow S_0)$ = 160 ns	
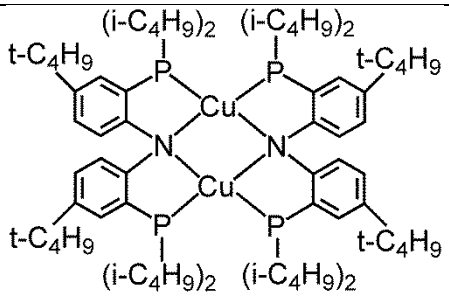 [Cu(PNP^{t}Bu)]$_2$ **16**	**$\Delta E(S_1\text{-}T_1)$ = 786 cm^{-1}** λ_{max}(300 K) = 512 nm Φ_{PL}(300 K) = 57 % τ(300 K) = 11 µs $\tau(T_1 \rightarrow S_0)$ = 343 µs $\tau(S_1 \rightarrow S_0)$ = 79 ns	[46]
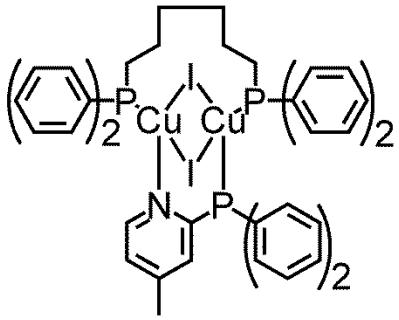 Cu_2I_2(MePyrPhos)(dpph) **17**	**$\Delta E(S_1\text{-}T_1)$ = 830 cm^{-1}** λ_{max}(300 K) = 519 nm Φ_{PL}(300 K) = 88 % τ(300 K) = 24 µs $\tau(T_1 \rightarrow S_0)$ = 110 µs $\tau(S_1 \rightarrow S_0)$ = 190 ns	[30,41]
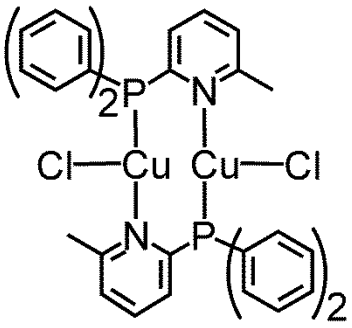 Cu_2Cl_2(N^P)$_2$ **18**	**$\Delta E(S_1\text{-}T_1)$ = 930 cm^{-1}** λ_{max}(300 K) = 485 nm Φ_{PL}(300 K) = 92 % τ(300 K) = 8.3 µs $\tau(T_1 \rightarrow S_0)$ = 42 µs $\tau(S_1 \rightarrow S_0)$ = 40 ns	[96,151]

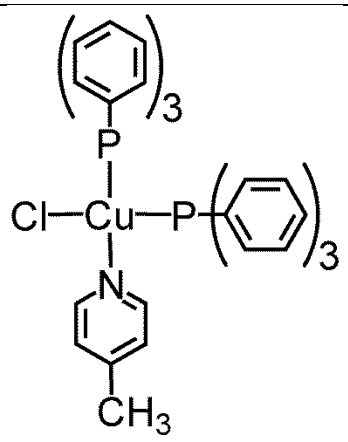 $CuCl(Pph_3)_2(4\text{-}Mepy)$ **19**	**$\Delta E(S_1\text{-}T_1) = 940\ cm^{-1}$** λ_{max}(300 K) = 468 nm Φ_{PL}(300 K) = 99 % τ(300 K) = 9.4 μs $\tau(T_1 \rightarrow S_0)$ = 34 μs $\tau(S_1 \rightarrow S_0)$ = 47 ns	[98]
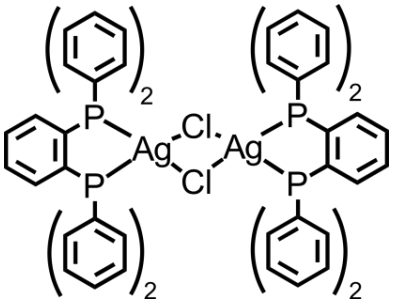 $Ag_2Cl_2(dppb)_2$ **20**	**$\Delta E(S_1\text{-}T_1) = 980\ cm^{-1}$** λ_{max}(300 K) = 480 nm Φ_{PL}(300 K) = 93 % τ(300 K) = 15 μs $\tau(T_1 \rightarrow S_0)$ = 1100 μs $\tau(S_1 \rightarrow S_0)$ = 45 ns	[107]
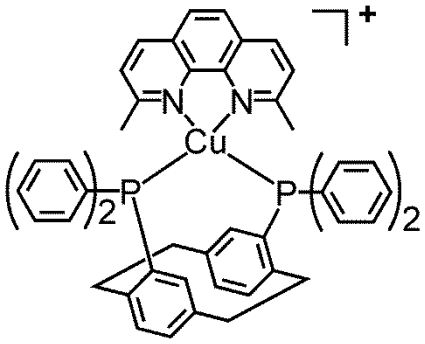 $Cu(dmp)(phanephos)^+$ **21**[c]	**$\Delta E(S_1\text{-}T_1) = 1000\ cm^{-1}$** λ_{max}(300 K) = 530 nm Φ_{PL}(300 K) = 80 % τ(300 K) = 14 μs $\tau(T_1 \rightarrow S_0)$ = 240 μs $\tau(S_1 \rightarrow S_0)$ = 40 ns	[92,152]

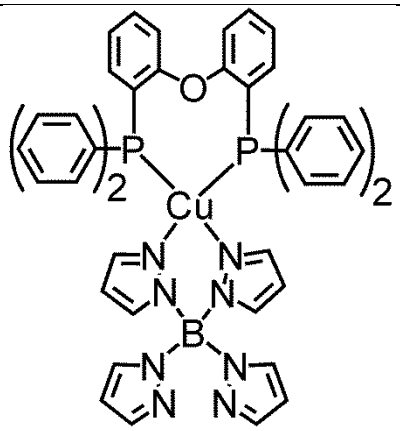 Cu(pop)(pz$_4$B) **22**	**$\Delta E(S_1\text{-}T_1)$ = 1000 cm^{-1}** λ_{max}(300 K) = 447 nm Φ_{PL}(300 K) = 90 % τ(300 K) = 22 µs $\tau(T_1 \rightarrow S_0)$ = 450 µs $\tau(S_1 \rightarrow S_0)$ = 80 ns	[95,149]
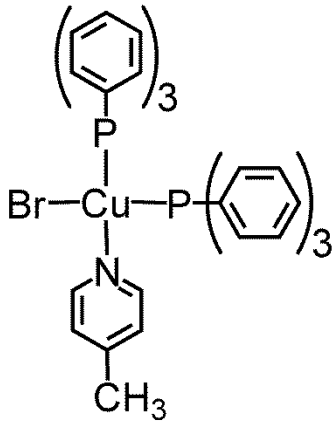 CuBr(Pph$_3$)$_2$(4-Mepy) **23**	**$\Delta E(S_1\text{-}T_1)$ = 1070 cm^{-1}** λ_{max}(300 K) = 467 nm Φ_{PL}(300 K) = 95 % τ(300 K) = 15 µs $\tau(T_1 \rightarrow S_0)$ = 50 µs $\tau(S_1 \rightarrow S_0)$ = 41 ns	[98]
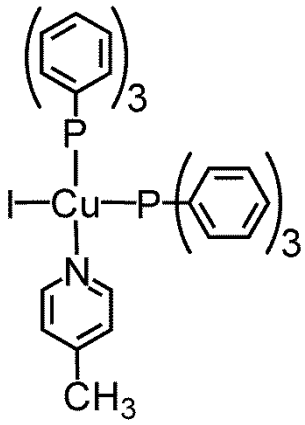 CuI(Pph$_3$)$_2$(4-Mepy) **24**	**$\Delta E(S_1\text{-}T_1)$ = 1170 cm^{-1}** λ_{max}(300 K) = 455 nm Φ_{PL}(300 K) = 66 % τ(300 K) = 9.5 µs $\tau(T_1 \rightarrow S_0)$ = 49 µs $\tau(S_1 \rightarrow S_0)$ = 14 ns	[98]

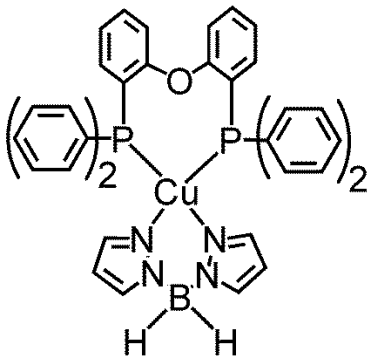 Cu(pop)(pz_2BH_2) **25**	**$\Delta E(S_1\text{-}T_1)$ = 1300 cm^{-1}** λ_{max}(300 K) = 436 nm Φ_{PL}(300 K) = 45 % τ(300 K) = 20 µs $\tau(T_1 \rightarrow S_0)$ = 610 µs $\tau(S_1 \rightarrow S_0)$ = 10 ns	[70,95,149]

a. Similar $\Delta E(S_1\text{-}T_1)$ values are expected to occur for all Ag(phen-substituted)(P_2-nCB) complexes displayed in this table.
b. Investigated as [Cu(tmbpy)(pop)](BF_4) powder.
c. Investigated as [Cu(dmp)(phanephos)](PF_6) powder.

3. Case study. TADF of a Cu(I) complex with large $\Delta E(S_1\text{-}T_1)$.

The luminescence properties of TADF compounds depend strongly on the energy separation between the lowest excited singlet and triplet state. In this case study, we discuss properties of Cu(dmp)(phanephos)$^+$ **21** (with dmp = 2,9-dimethyl-1,10-phenanthroline and phanephos = 4,12-bis(diphenylphosphino)-[2.2]-paracyclophane) (Figure 3).

DFT and TD-DFT calculations

Quantum mechanical DFT computations reveal that for this compound, the lowest excited states result dominantly from HOMO to LUMO transitions from metal and phosphorus orbitals to dmp ligand orbitals.[92] (Figure 3) Accordingly, the excited states have distinct admixtures of ^{1,3}MLCT character. This assignment is also supported by the photophysical investigations as discussed below. TD-DFT calculations, carried out in the T_1 state geometry, allow us to estimate an energy separation between the singlet and triplet MLCT states of $\Delta E(S_1\text{-}T_1) \approx 0.22$ eV. Since TD-DFT computations give energies of vertical transitions between Frank-Condon states, the calculated $\Delta E(S_1\text{-}T_1)$

value is overestimated as demonstrated experimentally (see below), but allows us to expect an occurrence of TADF at ambient temperature.

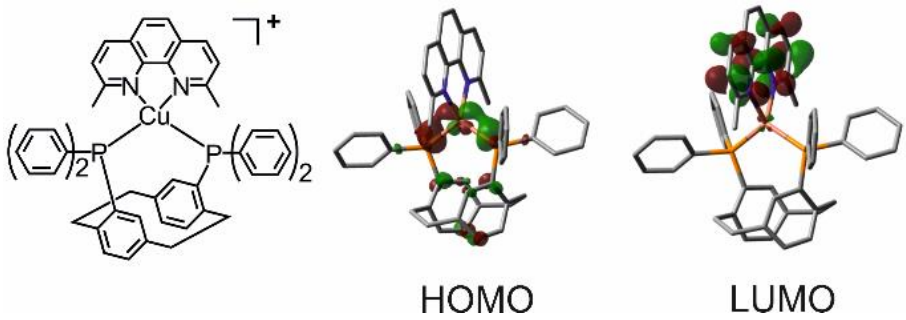

Figure 3. Chemical formula and frontier orbitals of Cu(dmp)(phanephos)$^+$ **21** obtained for the DFT-optimized triplet state (T_1) geometry. The calculations were performed at the B3LYP/def2-SVP[153-154] level of theory. Hydrogen atoms are omitted for clarity. HOMO and LUMO exhibit distinctly different spatial distributions. The HOMO is mainly composed of the copper 3d and phosphorus sp^3 atomic orbitals, while the LUMO represents essentially a π^* orbital of the dmp ligand.

Flattening distortions and non-radiative decay

An MLCT transition in Cu(I) complexes often leads to flattening distortions of the molecule in the excited state relative to the ground state geometry.[115,117-123,155-156] Such distortions are usually connected with an increase of non-radiative deactivations or even quenching of the emission due to a strong increase of the Franck-Condon factors of the low-lying vibrational modes of the excited state and the highly excited vibrational modes of the electronic ground state.[125-127] Thus, engineering of a highly emissive compound requires that such geometry changes are minimized. This can be achieved by using matrix materials characterized by cages of rigid micro-environments. In a different approach, the excited state distortions can also be reduced or even largely suppressed at the molecular level.

Cu(dmp)(phanephos)$^+$ **21** represents an example of a Cu(I) complex in which the excited state distortions are hindered owing to a rational molecular design. In particular, the diphosphine phanephos with a wide P-Cu-P bite angle of 116° [92] forms a rigid "semicage" for the metal ion coordinated by the second ligand. (Figure 4) Methyl groups

in the 2- and 9-positions of dmp exert steric demands that further hinder flattening distortions. Thus, mutual steric interactions of the chelating ligands strongly reduce flattening distortions and as a consequence radiationless relaxations.

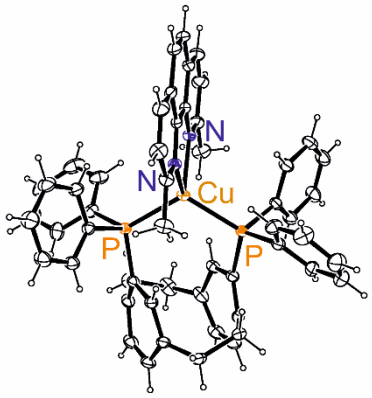

Figure 4. Perspective drawing of Cu(dmp)(phanephos)$^+$ **21** (enantiomer *R*) resulting from x-ray crystallography studies. Adapted from [92] with permission from The Royal Society of Chemistry.

Indeed, Cu(dmp)(phanephos)$^+$ **21** displays intense green-yellow luminescence at ambient temperature even in solution. (Figure 5) For instance, in dichloromethane the quantum yield Φ_{PL} is 40 %. (Table 2) With this Φ_{PL} value and the measured decay time of $\tau(CH_2Cl_2, 300\ K) = 10\ \mu s$ the nonradiative rate k^{nr} can be estimated, using the relation:

$$k^{nr} = (1 - \Phi_{PL})/\tau \qquad (2)$$

The resulting rate of $k^{nr} = 6.0 \cdot 10^4\ s^{-1}$ represents one of the smallest k^{nr} values found for Cu(I) complexes in liquid solution so far.[31] This proves the validity of the molecular design strategy applied to Cu(dmp)(phanephos)$^+$ **21**. The excited state distortions and thus, the extent of non-radiative relaxation can further be reduced by increasing the rigidity of the environment. Using the Φ_{PL} and τ data summarized in Table 2, the rates k^{nr} for a polymer matrix and a solid sample are found to be of $k^{nr} = 1.8 \cdot 10^4\ s^{-1}$ (PMMA) and $k^{nr} = 1.4 \cdot 10^4\ s^{-1}$ (powder), respectively. Interestingly, the changes of k^{nr} induced by the strongly different matrix rigidities are distinctly less than one order of magnitude.

This is regarded as being relatively small and it indicates that the excited state distortions are already partly suppressed at the level of molecular structure.

The discussed trend is also reflected by the small extent of spectral changes observed for the emission spectra. The emission maximum at T = 300 K of compound **21** is found at λ_{max} = 558 nm in dichloromethane. For the compound doped in PMMA it lies at λ_{max} = 535 nm and at 530 nm for a powder sample, respectively. Accordingly, the largest blue shift $\Delta\lambda_{max}$ (fluid solution $\rightarrow$ powder) amounts to $\Delta\lambda$(max) = 28 nm ($\approx$ 950 cm^{-1},118 meV) only. For comparison, for the blue-green emitting Cu(pop)(pz_2BH_2) **25**, $\Delta\lambda$(max) was found to be as large as 99 nm ($\approx$ 4200 cm^{-1}). [95] In the latter case, the large shift is related to the more flexible molecular structure that enables significant flattening distortions in the MLCT excited states. In compound **21**, such distortions are largely suppressed due to the large bite-angle and bulky phanephos ligand.

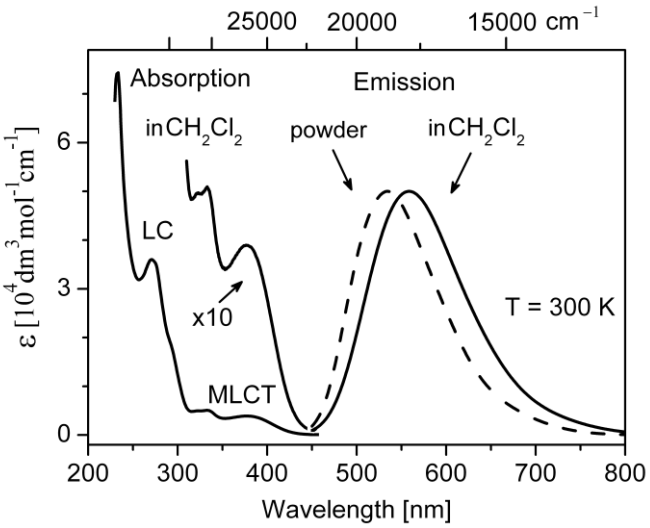

Figure 5. Ambient temperature absorption and emission spectra of Cu(dmp)(phanephos)$^+$ **21** recorded in diluted (c $\approx 3\cdot10^{-5}$ M^{-1}) dichloromethane solution (solid lines) and as [Cu(dmp)(phanephos)](PF_6) powder (dashed line). LC and MLCT denote ligand centered (π-π*) and metal-to-ligand charge-transfer (d-π*) transitions, respectively. Adapted from [92] with permission from The Royal Society of Chemistry.

Table 2. Luminescence properties of [Cu(dmp)(phanephos)](PF_6) **21** in dichloromethane, PMMA (poly(methyl methacrylate)), and as powder. Compare [92]

	T = 300 K					T = 77 K				
	λ_{max} [nm]	τ [μs]	Φ_{PL} [%]	k^r [s^{-1}]	k^{nr} [s^{-1}]	λ_{max} [nm]	τ [μs]	Φ_{PL} [%]	k^r [s^{-1}]	k^{nr} [s^{-1}]
CH_2Cl_2	558	10	40	$4.0 \cdot 10^4$	$6.0 \cdot 10^4$	548	130	60	$4.6 \cdot 10^3$	$3.1 \cdot 10^3$
PMMA	535	20	65	$3.3 \cdot 10^4$	$1.8 \cdot 10^4$	567	170	60	$3.5 \cdot 10^3$	$2.4 \cdot 10^3$
powder	530	14	80	$5.7 \cdot 10^4$	$1.4 \cdot 10^4$	562	240	70	$2.9 \cdot 10^3$	$1.3 \cdot 10^3$

TADF properties

As expected for a TADF material, the emission decay time τ is strongly dependent on temperature. (Table 2) Upon heating from T = 77 K to ambient temperature, the decay time becomes about one order of magnitude shorter with the quantum yield remaining approximately equally high. Thus, the change of τ is connected to a change of the radiative decay rate k^r. This rate is determined according to the following relation:

$$k^r = \Phi_{PL}/\tau \qquad (3)$$

In Table 2, radiative decay rates are given for different environments and temperatures, respectively. In particular, for the powder material k^r amounts to $2.9 \cdot 10^3$ s^{-1} at T = 77 K and increases with temperature increase to $5.7 \cdot 10^4$ s^{-1} at ambient temperature, i. e. by a factor of almost twenty. Thus, different emission mechanisms are active in the two temperature regimes.

The temperature dependence of the decay time is studied in more detail for a powder sample. (Figure 6) Between 20 K and about 120 K, the decay time is almost constant and as long as $\tau \approx 240$ μs (plateau). The assignment of this emission to a $T_1 \rightarrow S_0$ phosphorescence is straightforward. Obviously, in this plateau range no other decay mechanism is activated (thermal energy at ≈ 120 K amounts to ≈ 83 cm^{-1} or ≈ 10 meV). However, with further temperature increase, a steep decrease of the decay time is observed, which is due to the increase of the radiative decay rate k^r as discussed above. This change is related to a growing involvement of the higher lying S_1 singlet

state with its much higher decay rate of the transition to the electronic ground state S_0. The S_1 state is thermally activated from the lower lying T_1 state. Hence, the ambient temperature emission represents (largely) a thermally activated delayed fluorescence. (See also below.) It exhibits a decay time of τ(TADF) = 14 μs at 300 K.

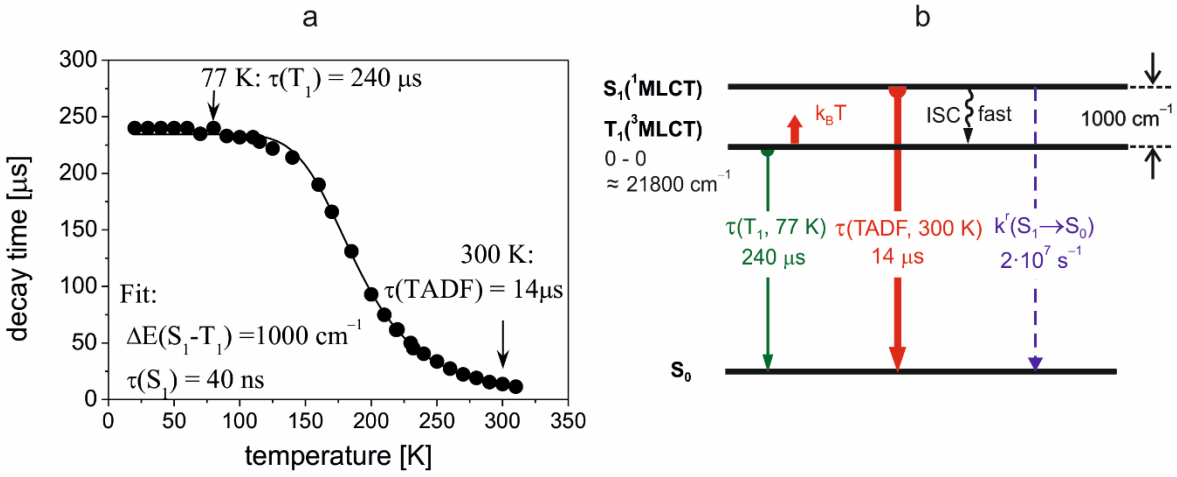

Figure 6. (a) Emission decay time of [Cu(dmp)(phanephos)](PF$_6$) **21** powder versus temperature. The emission was excited with a pulsed UV laser at λ_{exc} = 355 nm (pulse width 7 ns) and detected at λ_{det} = 550 nm. The solid line represents a fit of eq. (1) to the experimental data fixing the phosphorescence decay time $\tau(T_1)$ = 240 μs (plateau at 20 K < T < 120 K). The resulting fit parameters are $\Delta E(S_1\text{-}T_1)$ = 1000 cm^{-1} and $\tau(S_1)$ = 40 ns. τ(TADF) = 14 μs is the decay time of the delayed fluorescence at ambient temperature. (b) Energy level diagram for Cu(dmp)(phanephos)$^+$. The radiative rate for the $S_1 \rightarrow S_0$ transition $k^r(S_1 \rightarrow S_0)$ was determined according to eq. (3) assuming $\tau(S_1)$ = 40 ns (fit) and Φ_{PL} = 80 % (measured at ambient temperature). The energy of the $T_1 \rightarrow S_0$ 0-0 transition is estimated from the high energy flank of the 77 K emission spectrum (not reproduced). Compare [92]

The temperature dependence of $\tau = \tau(T)$, as displayed in Figure 6a, can be interpreted in terms of a three states kinetic model involving the electronic ground state S_0, the lowest triplet state T_1, and the lowest excited singlet state S_1, as expressed by eq. (1). By fitting this equation to the measured decay times and inserting the measured decay time $\tau(T_1)$ = 240 μs (plateau at 20 K < T < 120 K), values of $\tau(S_1)$ = 40 ns and $\Delta E(S_1\text{-}T_1)$ = 1000 cm^{-1} are obtained. The value of $\Delta E(S_1\text{-}T_1)$ = 1000 cm^{-1} corresponds well to the spectral blue shift of 1070 cm^{-1} observed for the emission maximum with

temperature increase from T = 77 K (λ_{max} = 562 nm) to 300 K (λ_{max} = 530 nm). (Table 2) This correspondence between the activation energy and the spectral shift upon temperature increase represents a further support for the assignment of the ambient temperature emission as TADF.

For completeness, it is remarked that the emission at ambient temperature frequently does not represent only TADF, but contains also some $T_1 \rightarrow S_0$ (phosphorescence) contribution. (Prompt fluorescence is not observed due to fast ISC of the order of a few tens of ps.[119,123,134-135,155,157-159] According to refs. [33,97], the intensity ratio $(S_1)/(T_1)$ can be expressed by:

$$\frac{I(S_1)}{I(T_1)} = \frac{k^r(S_1)}{k^r(I)+k^r(II)+k^r(III)} \cdot e^{-\frac{\Delta E(S_1-T_1)}{k_B T}} \qquad (4a)$$

With

$$k^r(T_1) = \frac{1}{3}(k^r(I)+k^r(II)+k^r(III)) \qquad (4b)$$

one obtains

$$\frac{I(S_1)}{I(T_1)} = \frac{k^r(S_1)}{3 \cdot k^r(T_1)} \cdot e^{-\frac{\Delta E(S_1-T_1)}{k_B T}} \qquad (4c)$$

k^r (I), k^r(II), and k^r(III) are the rates of transitions from the triplet substates I, II, and III of the lowest triplet state (T_1) to the ground state (S_0), respectively. $k^r(T_1) = k^r(T_1 \rightarrow S_0)$ represents the average transition rate from the three triplet sub-states to the ground state. We will return to the average decay properties later in section 4 (compare eq. (9). $k^r(S_1) = k^r(S_1 \rightarrow S_0)$ is the transition rate from the lowest excited singlet state (S_1) to the ground state, and $\Delta E(S_1-T_1)$ is the energy gap between states S_1 and T_1 (Compare [31,33]). For Cu(dmp)(phanephos)$^+$ **21** at T = 300 K with $\Delta E(S_1\text{-}T_1)$ = 1000 cm^{-1} (fit, Figure 6b), $k^r(S_1) = 2 \cdot 10^7$ s^{-1} (fit), and $k^r(T_1) = 2.9 \cdot 10^3$ s^{-1} (measured at 77 K; Table 2),

one obtains $I(S_1)/I(T_1) \approx 20$ Thus, the emission spectrum at ambient temperature is clearly dominated by TADF (≈ 95 % TADF, ≈ 5 % phosphorescence from T_1).

Radiative $S_1 \rightarrow S_0$ rate, absorption, and Strickler-Berg relation

The radiative rate $k^r(S_1)$ for the electronic transition between the excited singlet state S_1 and the ground state S_0 can be determined independently from an analysis of the absorption spectrum.[92] According to Figure 7, the absorption peak of lowest energy centred at ≈ 26300 cm^{-1} (380 nm) and showing a slight spectral overlap with the emission is assigned to the $S_0 \rightarrow S_1$ transition. Thus, a (radiative) transition rate for the related emission $S_1 \rightarrow S_0$ can be estimated using the well-known Strickler-Berg relation between the radiative decay rate of the spontaneous emission, and the strength of the corresponding absorption.[160] Accordingly, $k^r(S_1)$ can be expressed as:

$$k^r(S_1 \rightarrow S_0) = 8 \cdot \ln 10 \cdot \pi \cdot c \cdot n^2 \cdot N_A^{-1} \cdot \langle \bar{\nu}_{fl}^{-3} \rangle^{-1} \cdot \int \frac{\varepsilon(\bar{\nu}_{abs})}{\bar{\nu}_{abs}} d\bar{\nu}_{abs} \qquad (5)$$

where c is the speed of light in vacuum, N_A is the Avogadro number, and n is the refractive index of the medium. $\langle \bar{\nu}_{fl}^{-3} \rangle_{av}^{-1}$ displays the reciprocal of the mean value of the third power of the fluorescence energy $\bar{\nu}_{fl}$ [cm^{-1}] (weighted with the emission intensity at each $\bar{\nu}_{fl}$ value of the spectrum). The integral $\int \frac{\varepsilon(\bar{\nu}_{abs})}{\bar{\nu}_{abs}} d\bar{\nu}_{abs}$ represents the absorption strength of the $S_0 \rightarrow S_1$ band. $\varepsilon(\bar{\nu}_{abs})$ is the molar absorption (extinction) coefficient at a given energy $\bar{\nu}_{abs}$. If $\langle \bar{\nu}_{fl}^{-3} \rangle_{av}^{-1}$ is approximated by the third power of the emission maximum $\bar{\nu}_{max}^3$, eq. (5) can be rewritten as:

$$k^r(S_1 \rightarrow S_0) = const \cdot n^2 \cdot \bar{\nu}_{max}^3 \cdot \int \frac{\varepsilon(\bar{\nu}_{abs})}{\bar{\nu}_{abs}} d\bar{\nu}_{abs} \qquad (6)$$

with $const \approx 2.88 \cdot 10^{-12}$ s^{-1} mol cm.

From an integration of the lowest energy absorption band estimated by the shaded area as shown in Figure 7, a value of $\int \frac{\varepsilon(\bar{\nu}_{abs})}{\bar{\nu}_{abs}} d\bar{\nu}_{abs}$= 3.7·10^5 cm^2 mol^{-1} is obtained. Thus, for $\bar{\nu}_{max}$ = 17500 cm^{-1} (emission maximum in CH_2Cl_2 at ambient temperature and with n = 1.42) a spontaneous fluorescence rate of $k^r(S_1 \rightarrow S_0) \approx 1.2 \cdot 10^7$ s^{-1} is obtained. With respect to the different approximations made, this value corresponds reasonably well to the fluorescence decay rate of $k^r(S_1 \rightarrow S_0) \approx 2 \cdot 10^7$ s^{-1} as determined from the temperature dependence of the emission decay time as discussed above. (Figure 6)

The value of k^r lying in the range of 1 to 2·10^7 s^{-1} corresponds to a moderately allowed transition, as it is expected for a $S_0 \rightarrow {}^1$MLCT transition. The moderate allowedness of this transition is also reflected in the value of the small oscillator strength resulting from TD-DFT calculations (Figure 7). For the optimized singlet ground state geometry at the B3LYP/def2-SVP level of theory, the oscillator strength for the $S_0 \rightarrow S_1$ transition of f = 0.0621 is obtained. [92] With a simple relation, the radiative rate can be estimated according to: [125]

$$k^r \cong \bar{\nu}^2 f \qquad (7)$$

where $\bar{\nu}$ is the energy (in wavenumbers) corresponding to the maximum wavelength of absorption. With the calculated value of f = 0.0621 and the $S_0 \rightarrow S_1$ transition energy of 22670 cm^{-1} a radiative rate of 3·10^7 s^{-1} is estimated, being in agreement with the value of $k^r(S_1 \rightarrow S_0)$ = 2·10^7 s^{-1} as determined experimentally.

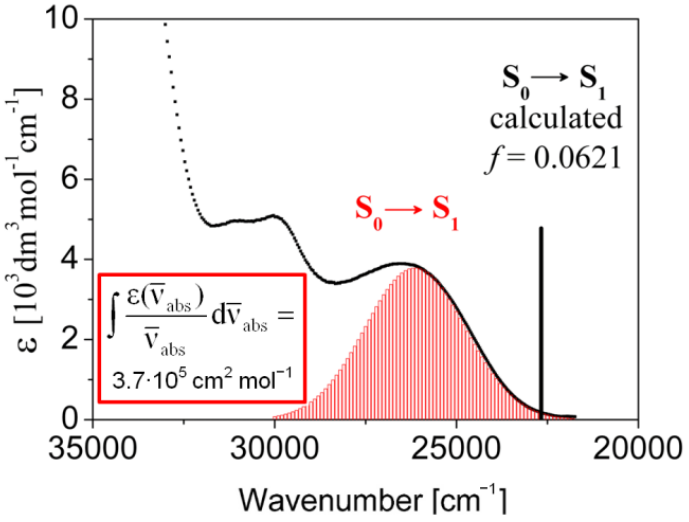

Figure 7. Absorption spectrum of Cu(dmp)(phanephos)$^+$ **21** in CH_2Cl_2 at ambient temperature. (Compare Figure 5) The red-shaded area approximates the lowest absorption. The integrated intensity is determined to $3.7 \cdot 10^5$ cm^2·mol^{-1}. The vertical line at $\bar{\nu} = 22670$ cm^{-1} represents the calculated energy of the $S_0 \rightarrow S_1$ MLCT transition with a relatively small oscillator strength of f = 0.0621. The TD-DFT calculation was performed for the ground state optimized geometry at the B3LYP/def2-SVP level of theory. Adapted from [92] with permission from The Royal Society of Chemistry.

With respect to the approximations made applying the different and independent methods, the $k^r(S_1 \rightarrow S_0)$ values ($2 \cdot 10^7$ s^{-1} from the decay time analysis, $1.2 \cdot 10^7$ s^{-1} from the absorption strength analysis, and $3 \cdot 10^7$ s^{-1} from a TD-DFT approach) are in good agreement. This is an important result, since it strongly supports the TADF assignment with respect to the involvement of the singlet S_1 state in the emission process at ambient temperature. Moreover, it is concluded that the geometry changes that still take place upon excitation do not significantly alter the $S_1 \rightarrow S_0$ transition rate determined for the relaxed geometry (from emission properties) as compared to the rate determined for the unrelaxed molecular geometry (from absorption).

4. Case study. TADF of a Cu(I) complex with small $\Delta E(S_1\text{-}T_1)$

As already addressed, Cu(I) complexes display a large variety of TADF properties. In particular, this is related to a large range of energy separations $\Delta E(S_1\text{-}T_1)$ between the

lowest singlet and triplet state being larger than 10^3 cm^{-1} (120 meV) or as small as a few hundred cm^{-1}. In section 3, a complex with a relatively large $\Delta E(S_1\text{-}T_1)$ was presented. In the present case study, we will focus on a complex characterized by a small $\Delta E(S_1\text{-}T_1)$ value and discuss related TADF properties.

DFT and TD-DFT calculations

In Figure 8, frontier orbital plots of Cu(dppb)(pz_2Bph_2) **2** (with dppb = 1,2-bis(diphenylphosphino)benzene and pz_2Bph_2 = diphenylbis(pyrazolylborate)) are reproduced together with the complex' chemical structure. The HOMO is derived from a metal 3d atomic orbital with significant contributions from the coordinating phosphorus and nitrogen atoms, whereas the LUMO is localized on the o-phenylene ring of the dppb ligand. Thus, similarly to Cu(dmp)(phanephos)$^+$ **21**, the orbitals display distinctly different spatial distributions and the related HOMO $\rightarrow$ LUMO excitations are of charge-transfer (CT) character. It can be further shown by TD-DFT calculations that the lowest excited singlet state S_1 and the triplet state T_1 are of more than 90% of HOMO-LUMO character.[96] Due to the distinct involvement of the metal, these states are assigned to largely represent ^{1}MLCT and ^{3}MLCT states, respectively. The significant spatial separation of HOMO and LUMO allows us to predict a relatively small exchange interaction and, thus, a small singlet-triplet energy separation $\Delta E(S_1\text{-}T_1)$. Indeed, TD-DFT calculations in the triplet state optimized geometry give a small value of $\Delta E(S_1\text{-}T_1)$ = 72 meV (≈ 580 cm^{-1}), estimated as the energy difference between vertical $S_0 \rightarrow S_1$ and $S_0 \rightarrow T_1$ transitions, [96] (Table 3) as being three times smaller than the value calculated for Cu(dmp)(phanephos)$^+$ **21**. Again, the $\Delta E(S_1\text{-}T_1)$ value calculated as the energy difference between the computed vertical excitations is overestimated. The experimentally determined activation energy amounts to $\Delta E(S_1\text{-}T_1)$ = 370 cm^{-1} (46 meV).

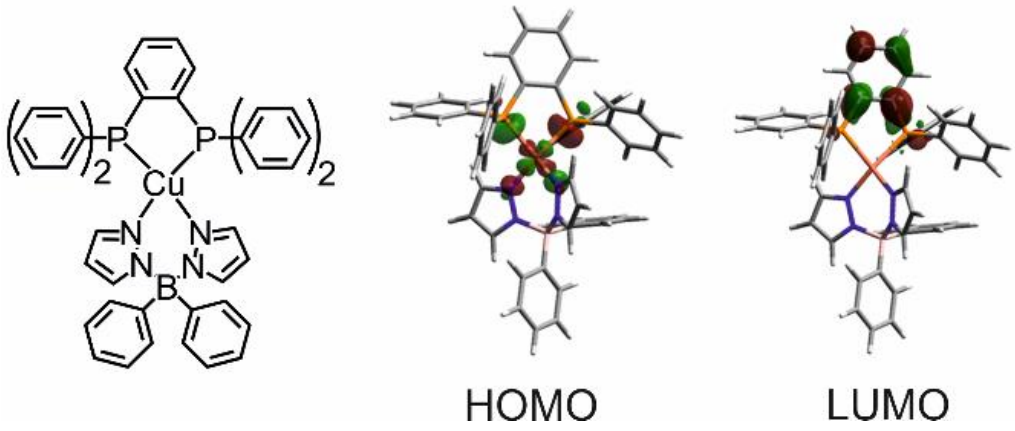

Figure 8. Chemical formula and contour plots of the HOMO and LUMO of Cu(dppb)(pz_2Bph_2) **2** resulting from DFT calculations for the triplet state geometry at the B3LYP/def2-SVP [153-154] level of theory. The frontier orbitals exhibit distinctly different spatial distributions. The HOMO is mainly composed of the copper 3d and phosphorus sp^3 atomic orbitals, while the LUMO represents a π^* orbital of the dppb ligand. Compare [96].

According to the spatial separation of the molecular orbitals involved in the transition between the electronic ground state S_0 and the lowest excited singlet state S_1 (^{1}MLCT), it can be predicted that the transition dipole moment and thus, the oscillator strength of the transition is relatively small. Indeed, TD-DFT calculations at the B3LYP/def2-SVP level of theory result to f = 0.0016, being more than one order of magnitude smaller than the value 0.0201 calculated for the $S_0 \rightarrow S_1$ transition of complex $[Cu(dmp)(phanephos)]^+$ **21**. Further results of TD-DFT calculations are presented in Table 3 that are later used to explain effects of SOC in complex **2**.

Table 3. Vertical transition energies, oscillator strengths, and main orbital contributions of selected electronic transitions of Cu(dppb)(pz_2Bph_2) **2** resulting from TD-DFT calculations for the optimized triplet state geometry (T_1 state) at the B3LYP/def2-SVP level of theory. [31,96] The lowest $S_0 \rightarrow S_n$ transition of HOMO-n → LUMO character that contains different Cu-3d character than the HOMO and that can exhibit SOC to the T_1 state is marked (see text).

Transition	Energy [eV]	oscillator strength	Main contribution
$S_0 \rightarrow T_1$	1.303	0	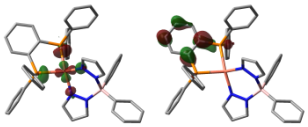 HOMO→LUMO
$S_0 \rightarrow T_2$	1.926	0	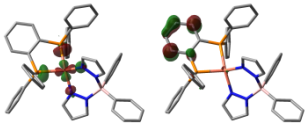 HOMO→LUMO+1
$S_0 \rightarrow T_3$	2.404	0	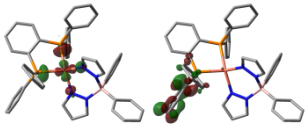 HOMO→LUMO+2
$S_0 \rightarrow T_4$	2.601	0	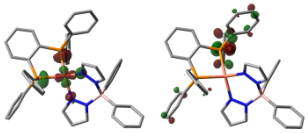 HOMO→LUMO+3
$S_0 \rightarrow T_5$	2.681	0	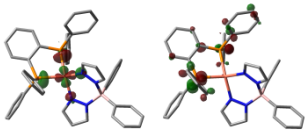 HOMO→LUMO+4
$S_0 \rightarrow S_1$	1.375	0.0016	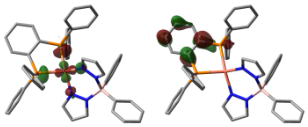 HOMO→LUMO
$S_0 \rightarrow S_2$	2.033	0.0038	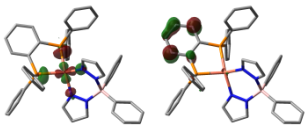 HOMO→LUMO+1
$S_0 \rightarrow S_3$	2.623	0.0547	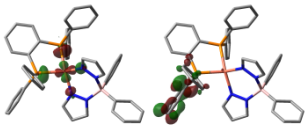 HOMO→LUMO+2

$S_0 \rightarrow S_4$	2.746	0.0253	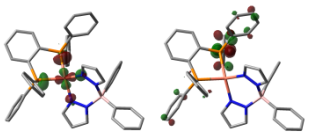	HOMO→LUMO+3
$S_0 \rightarrow S_5$	2.814	0.0727	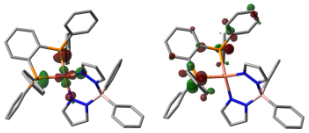	HOMO→LUMO+4
$S_0 \rightarrow S_6$ SOC[a]	2.848	0.0102	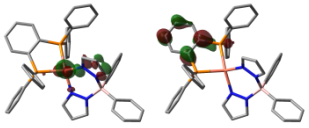	HOMO-1→LUMO

a. SOC to T_1 possible

Emission spectra and quantum yields

Emission properties of Cu(dppb)(pz_2BPh_2) **2** were studied for powder samples over a wide temperature range from T = 1.5 K to 300 K. Figure 9 displays representative emission spectra. Emission maxima, quantum yields, and decay times are collected in Table 4.

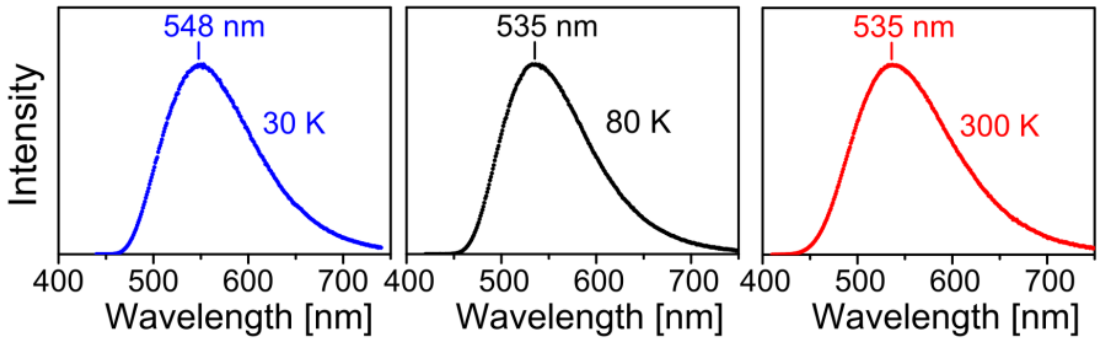

Figure 9. Luminescence spectra of Cu(dppb)(pz_2BPh_2) **2** powder recorded at different temperatures.[96]

Table 4. Emission data for a powder sample of Cu(dppb)(pz_2BPh_2) **2**.[96]

Temperature /K	λ_{max} /nm	Φ_{PL} /%	τ / μs	k^r /s^{-1} a	k^{nr} /s^{-1} a

300	535	70	3.3	$210 \cdot 10^3$	$9 \cdot 10^4$
80	535	≈100 [b]	300	$3.3 \cdot 10^3$	-
30	548	≈100 [b]	1200	$8.3 \cdot 10^2$	-

a. k^r and k^{nr} are determined by use of eqs. (2) and (3), respectively.
b. It is assumed that the quantum yield Φ_{PL} at T = 30 K amounts to 100 %, as determined experimentally at T = 77 K.

The compound shows intense green-yellow luminescence at all temperatures in the investigated range of 1.5 K to 300 K, with quantum yields Φ_{PL} of 70% at ambient temperature and about 100% at T = 77 K. The spectra are broad and unstructured, which correlates with the predicted MLCT character of the corresponding electronic transitions. With temperature increase to T ≥ 30 K, only a small blue shift is observed with the emission maximum λ(max) shifting from 548 nm at 1.5 K (not shown) and 30 K to 535 nm at 80 K and 300 K. This is a consequence of the thermal activation of the TADF decay path via the higher lying S_1 state above T ≈ 50 K (see below).

The triplet state T_1 and spin-orbit coupling

The emission spectra do not display distinct changes with temperature change. However, the decay kinetics varies drastically even at very low temperature (below T = 20 K). This is related to the properties of the triplet state and its substates. Therefore, before discussing effects of thermal activation of the singlet state, the TADF effect, we want to focus on triplet state properties.

At T = 1.5 K, the decay curve is distinctly non-monoexponential. The decay curve can be fitted with a bi-exponential function with the time constants of 7.7 ms and 470 µs. (Figure 10) These different decay constants are assigned to emissions from the three individual triplet T_1 substates I, II and III with $\tau_I \approx \tau_{II}$ = 7.7 ms and τ_{III} = 470 µs, respectively. It is remarked that for Cu(I) complexes, frequently a bi-exponential decay behavior is observed and not a tri-exponential one as expected for three triplet

substates [57,88,161-162] This is due to the fact that the decay times of two substates are often very similar.[33,95-97] Theoretical calculations based on SOC-TD-DFT (ADF2014) computations support this assignment. [163]

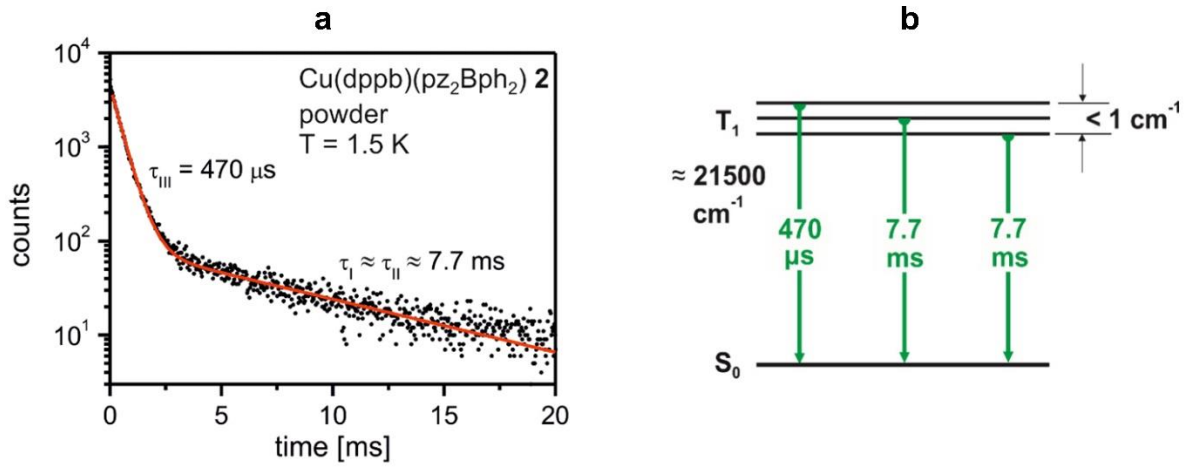

Figure 10. (a) Emission decay curve of Cu(dppb)(pz_2Bph_2) **2** at 1.5 K recorded for a powder sample after pulsed excitation at λ_{exc} = 372 nm and with signal detection at λ_{det} = 550 nm.[96] (b) Energy level scheme showing the triplet substates and the related decay paths at T = 1.5 K at vanishing fast equilibration.

At low temperature of T = 1.5 K, these T_1 substates are not thermally equilibrated due to slow spin-lattice relaxation (SLR). [57,88,138,161-162] This behavior is related to small zero-field splittings (ZFS) of the T_1 state of less than 1 or 2 cm^{-1} (0.1 or 0.2 meV).[9,57,70,88,161-162] Such a small ZFS value is a consequence of weak SOC of the T_1 substates with higher lying states. Furthermore, the emission decay time of $\tau(T_1)$ = 1200 µs (at 30 K) is extremely long if compared to Cu(dmp)(phanephos)$^+$ **21** (section 3) and many other Cu(I) complexes. [9,31,33,35,40,42,46,50,70,92,95-98,100,136,164-165]. Again, this is a consequence of the weak SOC with respect to the lowest triplet state.

Obviously, the (weak) allowedness of the $T_1 \rightarrow S_0$ transition is not dominantly related to the SOC constant of copper, which is with ζ = 857 cm^{-1} [166] not very small. More important is the extent of mixing of energetically higher lying singlet state(s). In a very simplified perturbational approach, the radiative rate can be described by [31,69-70,167]

$$k^r(T_1 \rightarrow S_0) \approx const \cdot \frac{\left|\left\langle S_m \left| H_{SO} \right| T_1 \right\rangle\right|^2}{\left|E(T_1) - E(S_m)\right|^2} \cdot \left|\left\langle S_0 \left| e\vec{r} \right| S_m \right\rangle\right|^2 \quad (8)$$

H_{SO} is the SO operator. $E(S_m)$ and $E(T_1)$ are the (unperturbed) energies of the (pure) singlet state S_m and the (pure) triplet state T_1, respectively. It this simple model, it is assumed that one higher lying singlet state S_m couples dominantly to the state T_1, i.e. to at least one T_1 triplet substate. $\left\langle S_0 \left| e\vec{r} \right| S_m \right\rangle$ is the dipole matrix element with the dipole operator $e\vec{r}$.

A discussion of the energy denominator and its size is particularly helpful. Presumably, SOC with the energetically most proximate singlet state of adequate character represents a leading contribution to the radiative rate. Therefore, eq. (8) shows only one mixing singlet state, being the state S_m, although several other singlet states may additionally contribute to the allowedness of the $T_1 \rightarrow S_0$ transition.

Quantum mechanical considerations show that SOC between a triplet state T_1 and a singlet state S_1 that both stem from the same orbital configuration, for example, from the HOMO→LUMO excitation, is negligible as for efficient SOC different d-orbitals must be involved in the coupling states. [9,30-31,69-72,75,168]

The TD-DFT calculations presented above for compound **2** show that the energetically nearest singlet state that involves another d-orbital than the T_1 state is the singlet state S_6. It originates from the HOMO−1 → LUMO electronic transition. According to Table 3, the energy separation that is responsible for dominant SOC amounts to $\Delta E(S_6–T_1)$ = 1.545 eV (≈ 12500 cm^{-1}) (ΔE(HOMO−(HOMO−1)) = 1.4 eV). As a consequence of this large energy denominator (eq. (8)), the triplet state does not experience effective SOC with state S_6. Hence, the phosphorescence decay time is expected to be very long. Indeed, this is found for compound **2** with $\tau(T_1 \rightarrow S_0)$ = 1200 µs. For comparison, the phosphorescence decay time of a compound that exhibits a much smaller energy

denominator is given: For example, $Cu_2Cl_2(N^P)_2$ **18** with an energy separation between HOMO and HOMO−1 (that involve different d-orbitals) amounts to only 0.378 eV (3000 cm^{-1}). [31,97] Since this HOMO-1 → LUMO excitation essentially defines the S_2 state, the energy separation to the T_1 state is much smaller than for compound **2**. Accordingly, the mixing of S_2 and T_1 becomes distinctly stronger (eq. (8)) and, hence, the triplet decay time amounts to only $\tau(T_1 \rightarrow S_0)$ = 43 µs.[31,97] Thus, the $T_1 \rightarrow S_0$ allowedness of compound **18** is by a factor of almost 30 higher than found for compound **2**.

The size of the squared dipole matrix element $\langle S_0 | e\vec{r} | S_m \rangle$ with the dipole operator $e\vec{r}$ is also of importance for the radiative rate $k^r(T_1 \rightarrow S_0)$ (or more exactly for the rate of the individual triplet substate that mixes with S_m). The corresponding value is proportional to the oscillator strength or the molar absorption coefficient of the singlet-singlet transition $S_0 \rightarrow S_m$, whereby S_m is the singlet state that can mix with the T_1 state via SOC.[69,72] With respect to the corresponding allowedness it is referred to Table 3.

For completeness, it is remarked that literature discussions frequently assume dominating SOC between T_1 and S_1. However, for compound **2**, the corresponding energy separation is very small amounting to only $\Delta E(S_1-T_1)$ = 370 cm^{-1} (See below). As a consequence, relatively strong SOC would be expected to occur. Above, it has been demonstrated that this is not the case. Obviously, the simple literature approach is not suited.

Temperature dependence of the emission decay time and TADF

Let us focus on the temperature dependence of the emission decay time. With temperature increase, the SLR processes become faster (presumably according to a Raman process of spin-lattice relaxation (SLR) [138-139,161]) resulting in a fast thermalization of the three T_1 substates. At sufficiently high temperature, e.g. above T =

10 or 20 K, an average emission decay time τ_{av} is normally observed as expressed by eq. (9): [9,33,57,70,88,95-96,138,140,162]

$$\tau_{av} = 3\left(\tau_{I}^{-1} + \tau_{II}^{-1} + \tau_{III}^{-1}\right)^{-1} \quad (9)$$

Inserting the decay times of $\tau_I \approx \tau_{II}$ = 7.7 ms and τ_{III} = 470 µs, as determined at T = 1.5 K, one obtains τ_{av} = 1250 µs. Almost the same value of $\tau(T_1)$ = 1200 µs (monoexponential decay) is measured at T = 30 K. (Figure 11). Thus, the assignments of the decay times we made above are validated.

Figure 11 displays emission decay curves and the temperature dependence of the decay time for the range of 20 K ≤ T ≤ 300 K. From T = 20 K to about 40 K the decay time remains constant (plateau) with $\tau(T_1)$ = 1200 µs. With further temperature increase the decay time decreases drastically to τ(80 K) = 300 µs and τ(300 K) = 3.3 µs. The plot of the measured τ values versus temperature has a characteristic form of an s-shaped curve similar to the one obtained for Cu(dmp)(phanephos)$^+$ **21** (Figure 6a) but with the point of maximum slope shifted from 180 K to 70 K for compound **2**. The radiative rate k^r, determined by use of eq. (3), rises from the low temperature value of k^r(30 K) = $8.3\cdot10^2$ s^{-1} to k^r(80 K) = $3.3\cdot10^3$ s^{-1} and to k^r(300 K) = $2.1\cdot10^5$ s^{-1}, respectively. (Table 4) The latter value represents a rate increase by a factor of 250 as compared to the k^r(30 K) value. This drastic increase of the radiative rate combined with the spectral blue shift of 13 nm with temperature increase (Figure 9) is explained by an involvement of a higher lying state that carries a higher radiative rate, hence demonstrating the occurrence of TADF.

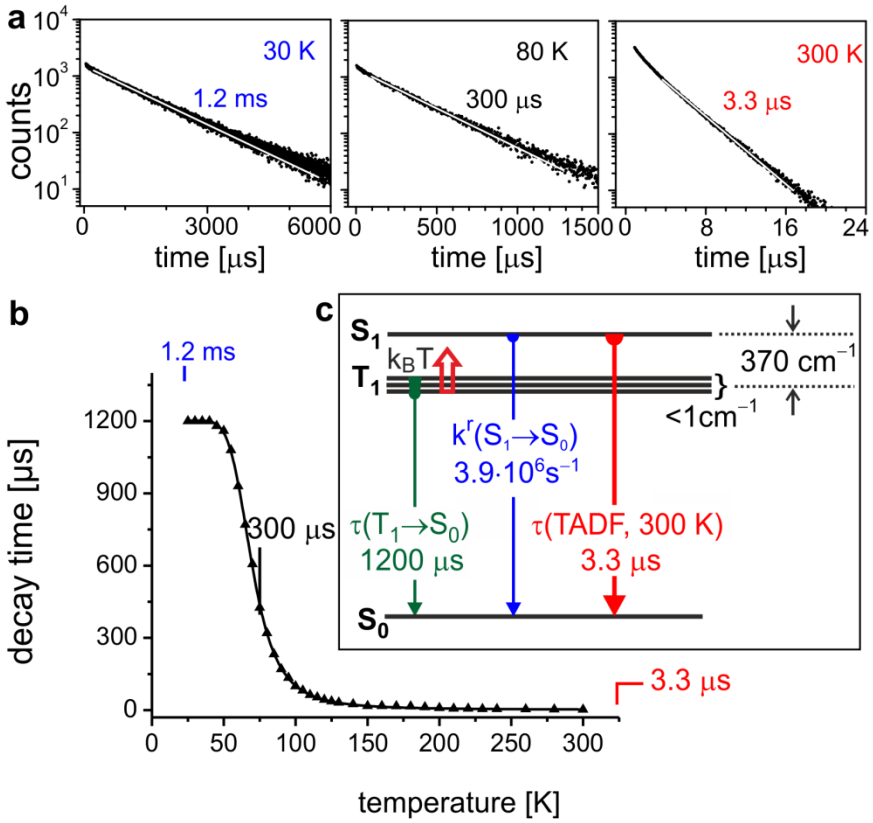

Figure 11. (a) Emission decay profiles of Cu(dppb)(pz_2Bph_2) **2** (powder) at 30, 80, and 300 K recorded after pulsed excitation at λ_{exc} = 378 nm and detected at λ_{det} = 540 nm. (b) Emission decay time τ versus temperature. The solid line represents a fit of eq. (1) to the experimental $\tau(T)$ values fixing $\tau(T_1)$ = 1.2 ms as measured at T = 30 K. The fit parameters are $\tau(S_1)$ = 180 ns and $\Delta E(S_1\text{-}T_1)$ = 370 cm^{-1}, respectively. (c) Energy level diagram of Cu(dppb)(pz_2Bph_2) **2**. Both competing emission processes are marked: Phosphorescence with a decay time of $\tau(T_1)$ = 1.2 ms dominating the photophysical behavior at temperatures below about 50 K and TADF determining the emission properties at higher temperatures with a measured decay time at 300 K of 3.3 µs (with the emission quantum yield of Φ_{PL}= 70%). [96]

An analysis of the decay time data according to the Boltzmann-type eq. (1), leads to an activation energy of $\Delta E(S_1\text{-}T_1)$ = 370 cm^{-1} and a prompt fluorescence decay rate of $k^r(S_1 \rightarrow S_0) = 3.9 \cdot 10^6\ s^{-1}$ (taking the emission quantum yield of Φ_{PL}= 70 % as measured at 300 K into account).[1] (Figure 11) Again, it is stressed that the prompt fluorescence

[1] For completeness, it is remarked that the value of $k^r(S_1 \rightarrow S_0) = 3.9 \cdot 10^6\ s^{-1}$ represents a coarse estimate, since eq. (1) is only valid, if the parameters in this equation, $k(T_1)$, $k(S_1)$, and $\Delta E(S_1\text{-}T_1)$, are independent of temperature. This is not strictly the case, since the emission quantum yield decreases with temperature. However, an alternative fit can be applied when we restrict the temperature range for the fit procedure to 30 ≤ T ≤ 150 K. Then it is reasonable to assume constant parameters, in particular, the emission quantum yield should be almost constant, i. e. ≈ 100 % as measured at T = 80 K. [96] For this restricted fit range, essentially the same fit parameters are obtained as discussed above. For this situation, we find $\tau(S_1)$ = 180 ns at Φ_{PL}= 100 % and a rate of $k^r(S_1) = 5.6\ 10^6\ s^{-1}$.

could not be observed directly in our experiments conducted with ns time resolution. This agrees with measured ISC time of the order of several ps. [119,123,135,155,157-159] The resulting energy level diagram and the relevant rates are summarized in Figure 11c.

The value of $\Delta E(S_1\text{-}T_1)$ = 370 cm^{-1} represents one of the smallest splitting values found so far. [31,96] Accordingly, Cu(dppb)(pz_2Bph_2) **2** shows a very short TADF decay time of τ(TADF) = 3.3 µs, being one of the shortest values reported so far for Cu(I) complexes (Compare section 6).

The experimental characterization of the luminescence behavior of Cu(dppb)(pz_2Bph_2) **2** supports the predictions based on model calculations, as developed above. According to the distinct spatial separation of the orbitals involved in the lowest excited states, the (formal) fluorescence decay time of $\tau(S_1)$ = 180 ns (calculated from $k^r(S_1 \rightarrow S_0) = 3.9 \cdot 10^6$ s^{-1} and Φ_{PL}= 70%) is relatively long for a spin-allowed transition. For instance, it is about four times longer than the decay time of the S_1 state as determined for Cu(dmp)(phanephos)$^+$ **21**. (Section 3) A large difference of the $\tau(S_1)$ lifetimes could be predicted by the TD-DFT calculations, as the oscillator strength of the corresponding $S_0 \rightarrow S_1$ transition, being 0.0016 for Cu(dppb)(pz_2Bph_2) **2** (Table 3), is more than an order of magnitude smaller than calculated for Cu(dmp)(phanephos)$^+$ **21** with f = 0.0201 (section 3).

Interestingly, the case studies presented in sections 3 and 4 focusing on two complexes with very different allowedness of the $S_1 \leftrightarrow S_0$ transitions is displayed inversely in the size of the energy splitting $\Delta E(S_1\text{-}T_1)$. For Cu(dmp)(phanephos)$^+$ **21,** it amounts to 1000 cm^{-1} (120 meV), while for Cu(dppb)(pz_2Bph_2) **2** a value of 370 cm^{-1} (46 meV) is found. This important relation will be addressed in section 5.

Moreover, the photophysical studies presented in sections 3 and 4 reveal an important practical conclusion concerning the assignments of emission processes. Both compounds show a phosphorescence plateau at low temperatures, at T < 120 K in the

case of Cu(dmp)(phanephos)$^+$ **21** with $\Delta E(S_1\text{-}T_1)$ = 1000 cm^{-1} and at T < 50 K in the case of Cu(dppb)(pz_2Bph_2) **2** with $\Delta E(S_1\text{-}T_1)$ = 370 cm^{-1}, respectively. At ambient temperature, the emission of both compounds represents TADF. Importantly, in many laboratories only two temperature regimes of T = 300 K (ambient temperature) and T = 77 K (boiling point of nitrogen) are easily accessible. Therefore, characterization of new compounds is usually performed at these two temperatures. Based on these results, preliminary conclusions concerning the character of the emissive states and the emission mechanism(s) are drawn. For Cu(dmp)(phanephos)$^+$ **21**, with the measured decay time of τ(77 K) = 240 μs (plateau range between 20 K and 120 K) and τ(300 K) = 14 μs, respectively, the emissions at low temperature and at ambient temperature would be assigned correctly as phosphorescence from the T_1 state and as TADF, respectively. For Cu(dppb)(pz_2Bph_2) **2** with τ(77 K) = 300 μs and τ(300 K) = 3.3 μs, a similar assignment would not be correct. As shown in Figure 11, the phosphorescence decay time $\tau(T_1)$ = 1200 μs (plateau for T $\leq$ 40 K) is four times longer than found at 77 K. Thus, the emission at 77 K cannot be assigned as phosphorescence. On the contrary, it represents mainly delayed fluorescence (TADF) even at T = 77 K. The TADF to phosphorescence ratio is estimated (by use of eq. 4c) to 75% to 25%. Correspondingly, emission spectra recorded at T = 77 K and 300 K are not shifted with respect to each other as for the two temperatures the spectral maxima of compound **2** are found at 535 nm. Thus, conclusions made on the basis of 77 K and ambient temperature measurements must be taken with care. The risk of possible misinterpretation is particularly large when the energy separation $\Delta E(S_1\text{-}T_1)$ is small.

5. Energy separation $\Delta E(S_1\text{-}T_1)$ and $S_1 \rightarrow S_0$ fluorescence rate

In section 2, it was already shortly discussed that a reduction of the energy separation between the lowest singlet S_1 and triplet T_1 state is connected with a decrease of the

radiative singlet-singlet rate $k^r(S_1 \rightarrow S_0)$. This relation has also been addressed in the two previous sections based on case studies. Since both photophysical parameters crucially determine the TADF behavior, in particular, the TADF decay time, we want to focus in this section on a simple model that may explain this relation.

Experimental correlation between $\Delta E(S_1\text{-}T_1)$ and $k^r(S_1 \rightarrow S_0)$ for Cu(I) compounds

During the last years, the $\Delta E(S_1\text{-}T_1)$ energy separations and the $S_1 \rightarrow S_0$ fluorescence decay times have been determined for a large number of Cu(I) compounds that show TADF. Both parameters result from fit procedures by use of eq. (1). For two compounds, this has been discussed in detail in sections 3 and 4. It is stressed again that the prompt fluorescence was not observed directly, but the corresponding $k^r(S_1 \rightarrow S_0)$ rate could be determined. In Table 5, adapted from Ref. [31] , we summarize the corresponding data for Cu(I) compounds. The fitting procedure leads to the formal (prompt) decay time $\tau(S_1)$ or to the rate $k(S_1 \rightarrow S_0)$. From this information and by use of the measured photoluminescence quantum yield Φ_{PL} one can easily determine the radiative rate $k^r(S_1 \rightarrow S_0)$ applying eq. (3).

Table 5. Energy separation $\Delta E(S_1\text{-}T_1)$ and radiative rate $k^r(S_1 \rightarrow S_0)$ determined by fitting procedures applying eq. (1) to experimental decay time data. $\tau(S_1)$ is the (formal) prompt fluorescence decay time and Φ_{PL} the emission quantum yield. Adapted from ref. [31].

	Compound	$\Delta E(S_1–T_1)$ [cm^{-1}]	$\tau(S_1)$ [ns]	Φ_{PL} (300 K)	$k^r(S_1 \rightarrow S_0)$ [10^6 s^{-1}]	Refs.
1	Cu_2I_2[MePyrPHOS)$(Pph_3)_2$	270	570	0.97	1.7	[30]
2	Cu(dppb)(pz_2Bph_2)	370	180	0.70	3.9	[96]
3	$[Cu(\mu\text{-}Cl)(PNMe_2)]_2$	460	210	0.45	2.1	[33]
4	$[Cu(\mu\text{-}Br)(PNMe_2)]_2$	510	110	0.65	5.9	[33]
5	$[Cu(\mu\text{-}I)(PNMe_2)]_2$	570	90	0.65	7.2	[33]
6	$Cu_2Cl_2(dppb)_2$	600	70	0.35	5.0	[107]

7	$[Cu(\mu\text{-}I)(PNpy)]_2$	630	100	0.65	6.5	[33]
8	$Cu(pop)(pz_2BPh_2)$	650	170	0.9	5.3	[9,95]
14	$Cu(tmbpy)(pop)^+$	720	160	0.55	3.4	[35]
15	$(IPr)Cu(py_2\text{-}BMe_2)$	740	160	0.76	4.8	[34]
16	$[Cu(PNP^tBu)]_2$	786	79	0.57	7.2	[46]
17	$Cu_2I_2(MePyrPHOS)(dpph)$	830	190	0.88	4.6	[30]
18	$Cu_2Cl_2(N\text{^}P)_2$	930	40	0.92	23	[97]
19	$CuCl(Pph_3)_2(4\text{-}Mepy)$	940	47	0.99	21	[98]
21	$Cu(dmp)(phanephos)^+$	1000	40	0.80	20	[92]
22	$Cu(pop)(pz_4B)$	1000	80	0.9	11	[95]
23	$CuBr(Pph_3)_2(4\text{-}Mepy)$	1070	41	0.95	23	[98]
24	$CuI(Pph_3)_2(4\text{-}Mepy)$	1170	14	0.66	47	[98]
25	$Cu(pop)(pz_2BH_2)$	1300	10	0.45	45	[70,95]

In Figure 12, the $k^r(S_1 \rightarrow S_0)$ data are plotted versus $\Delta E(S_1-T_1)$. It is obvious that with decreasing energy splitting the allowedness of the $S_1 \rightarrow S_0$ transition decreases drastically. For example, if compound **25** is compared to compound **1**, $\Delta E(S_1-T_1)$ decreases from 1300 cm^{-1} to 270 cm^{-1}, while the allowedness of the $S_1 \rightarrow S_0$ transition decreases by a factor of about 26. In a simple consideration, using eq. (1), it can be seen that the TADF decay time will not become shorter, when $\Delta E(S_1-T_1)$ reaches 300 − 200 cm^{-1} (≈ 40 or 25 meV). Such a minimum decay time lies in the range of several µs [169], at least for the type of Cu(I) compounds discussed here.

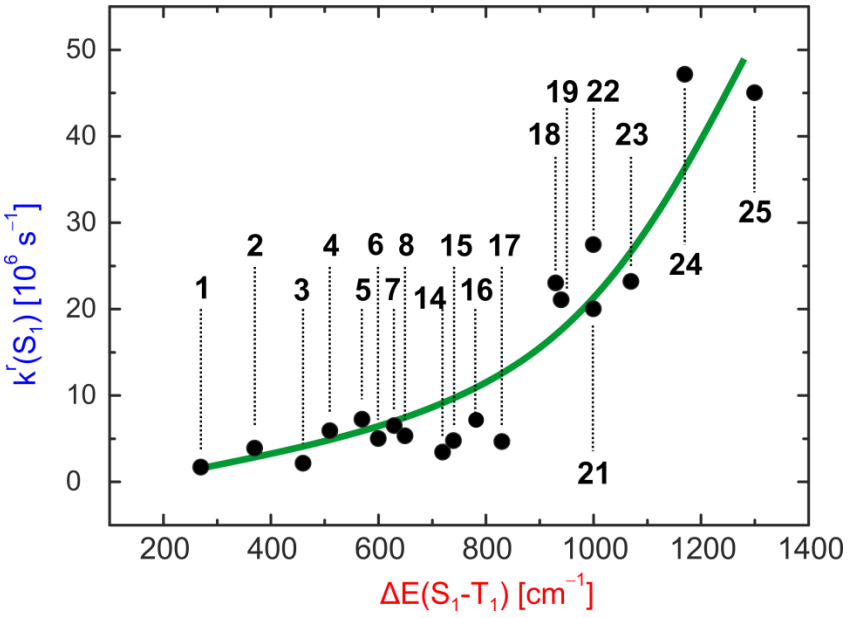

Figure 12. Radiative decay rate $k^r(S_1\text{-}S_0)$ plotted versus $\Delta E(S_1\text{-}T_1)$ for different Cu(I) complexes that show TADF at ambient temperature (data from Table 5). The fit curve represents an exponential function as guide for the eye. Adapted from ref. [31].

Quantum mechanical considerations

In this section, we want to illustrate on a simple quantum mechanical basis, following [31], why a small energy separation $\Delta E(S_1\text{-}T_1)$ between the lowest singlet S_1 and triplet T_1 state is related to a small radiative rate of the $S_1 \rightarrow S_0$ transition, i.e. a small $k^r(S_1 \rightarrow S_0)$ value. Let us assume that S_1 and T_1 can be described by a one-electron transition from HOMO φ_H to LUMO φ_L. In this situation, simple expressions can be given for the radiative rate $k^r(S_1\text{-}S_0)$ (= $k^r(S_1 \rightarrow S_0)$) and the energy splitting $\Delta E(S_1\text{-}T_1)$.

The radiative rate may be obtained from the transition dipole moment $\vec{\mu}(S_1 - S_0)$, which is approximately given by

$$\vec{\mu}_{H,L} = e\int \varphi_H(\vec{r})\vec{r}\varphi_L(\vec{r})d^3r = e\int \varphi_H(\vec{r})\varphi_L(\vec{r})\vec{r}d^3r \qquad (10)$$

$\vec{r}$ is the dipole vector and e is the electron charge.

Thus, the radiative rate can be expressed by (see ref. [170] p. 159]), [31]:

$$k^r(S_1 - S_0) = 2C\nu^3 n^3 \left|\vec{\mu}_{HL}\right|^2 \qquad (11)$$

$$k^r(S_1 - S_0) = 2e^2 C \nu^3 n^3 \left| \int \varphi_H(\vec{r}) \varphi_L(\vec{r}) \vec{r} d^3 r \right|^2 \qquad (12)$$

with the numerical constant $C = 16\pi^3 / (3\varepsilon_0 h c^3)$

wherein ε_0 is the vacuum permittivity, h is Planck´s constant, and c the velocity of light. $\upsilon = \Delta E(S_1\text{-}S_0)/h$ is the transition frequency and n the refractive index.

The energy separation $\Delta E(S_1\text{-}T_1)$ can be expressed in this approximation by twice the exchange integral K_{HL} for HOMO and LUMO (See ref. [131] p. 86) giving

$$\Delta E(S_1\text{-}T_1) \approx 2K_{HL} \qquad (13)$$

with

$$K_{HL} = \frac{e^2}{4\pi\varepsilon_0} \int \varphi_H(\vec{r}_1) \varphi_L(\vec{r}_2) \frac{1}{|\vec{r}_2 - \vec{r}_1|} \varphi_H(\vec{r}_2) \varphi_L(\vec{r}_1) d^3 r_1 d^3 r_2 \qquad (14)$$

or

$$K_{HL} = \frac{e^2}{4\pi\varepsilon_0} \int \varphi_H(\vec{r}_1) \varphi_L(\vec{r}_1) \frac{1}{|\vec{r}_2 - \vec{r}_1|} \varphi_H(\vec{r}_2) \varphi_L(\vec{r}_2) d^3 r_1 d^3 r_2 \qquad (15)$$

It is an important result that both the exchange interaction and hence the energy splitting $\Delta E(S_1\text{-}T_1)$ (eq. (13)) as well as the radiative rate (eq. (12)) depend quadratically on the product of $\varphi_H(r)\varphi_L(r)$ or the squared overlap of HOMO and LUMO[2]. Accordingly, it becomes obvious that $\Delta E(S_1{-}T_1)$ and $k^r(S_1{\rightarrow}S_0)$ correlate: A small HOMO−LUMO overlap implies small $\Delta E(S_1{-}T_1)$ and small $k^r(S_1{\rightarrow}S_0)$. This relation is schematically illustrated in Figure 13.

[2] It is noted that the modified overlap $\int |\varphi_H||\varphi_L| dV$ is a quantitative measure for the spatial overlap.[171]

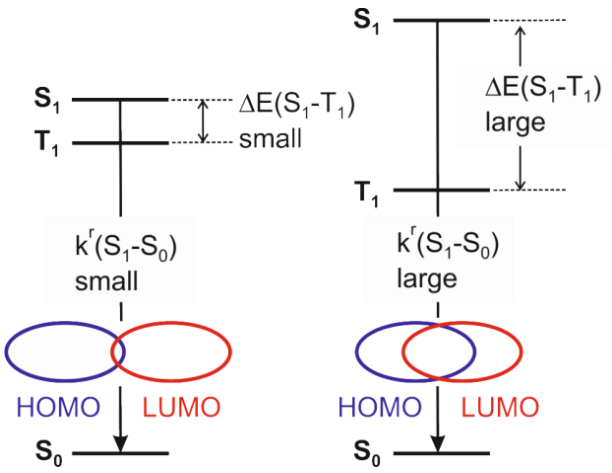

Figure 13. Schematic illustration of the relation between energy splitting $\Delta E(S_1\text{-}T_1)$ and the radiative decay rate $k^r(S_1\text{-}S_0)$ on the spatial overlap of HOMO and LUMO. Reproduced from Ref. [31] with permission from Coord. Chem. Rev. (Elsevier).

The simple qualitative model presented above allows us to understand the experimental results as displayed in Figure 12. The model´s basic assumption is that the low-lying singlet S_1 and triplet T_1 states, originating from the HOMO→LUMO excitation, are energetically well separated from higher lying energy states. Accordingly, in the scope of this material class (or this model) we cannot reduce the TADF decay time distinctly below a few µs. However, the simple model does not contain mixing of the singlet state S_1 with a higher lying singlet state that carries high oscillator strength with respect to the transition to the electronic ground state. Such mixing, induced by configuration interaction (CI), might significantly increase the radiative rate of the lowest singlet-singlet transition without strongly alter the energy splitting $\Delta E(S_1-T_1)$. Presumably, such Cu(I) complexes may be developed in future. In section 6, we will address this challenge shortly again.

6. Design strategies for highly efficient Ag(I)-based TADF compounds.

In contrast to Cu(I) complexes, TADF materials based on Ag(I) are rarely reported. [104,106-109] This is related to the higher oxidation potential of Ag^+ compared to Cu^+.[172] Accordingly, the 4d-orbitals of Ag(I) complexes lie mostly energetically below ligand-

centered (LC) orbitals. As a consequence, low-lying states of ^{3}LC character determine the emission properties. [106,173-176] Thus, Ag(I) complexes often do not exhibit TADF, but long-lived phosphorescence and sometimes even slow intersystem crossing.[175] Therefore, designing Ag(I) complexes that show TADF represents an optimization task. In this respect, it is required to destabilize the energetically lower-lying 4d-orbitals by an organic ligand with good electron-donating ability. This may be attainable with electron-donating bidentate phosphine ligands. Indeed, it has already been demonstrated that this strategy is successful. For example, $Ag_2Cl_2(dppb)_2$ **20** represents a blue light emitting material that shows efficient TADF with Φ_{PL} = 97%, though with a relatively long decay time of τ(TADF, 300 K) = 15 μs (Table 1).[107] Another attractive ligand is *nido*-carborane-bis-(diphenylphosphine) (P_2-nCB). [177] It coordinates via phosphine groups and thus, induces substantial electron-donating character. Additionally, electron donation is strongly enhanced by the negative charge of the *nido*-carborane moiety. Suitable complexes can be built using the (P_2-nCB) ligand in combination with 1,10-phenanthroline (phen) or substituted phen ligands. Accordingly, a series of neutral Ag(I) complexes, referring to the numbers from **9** to **13**, is obtained (Table 1).[108-109] In this section, we want to focus on these Ag(phen)(P_2-nCB) type compounds and to demonstrate key steps for designing a material that shows TADF behavior. Interestingly, by this strategy an efficiency breakthrough is reached.[108-109]

Ag(phen)(P_2-nCB) – A first step to achieve TADF

DFT and TD-DFT calculations give an insight into electronic properties of Ag(phen)(P_2-nCB) **9**. The chemical structure as well as HOMO and LUMO plots are displayed in Figure 14. The calculations were performed for the optimized triplet T_1 state geometry. From the TD-DFT approach, it is indicated that the states S_1 and T_1 are dominated by HOMO→LUMO electronic transitions by 96 % and 94 %, respectively. Analysis of the

frontier orbitals shows that the HOMO is mainly localized on the phosphines and the silver ion, whereas the LUMO is localized on the phen ligand. Accordingly, both states may be assigned to be of (metal + ligand L) to ligand L' charge transfer (^{1,3}MLL'CT) character. The small overlap of HOMO and LUMO suggests the occurrence of a small exchange interaction between the unpaired electrons and thus, a small $\Delta E(S_1\text{-}T_1)$ splitting. From TD-DFT calculations the energy gap of $\Delta E(S_1\text{-}T_1)$ = 1070 cm^{-1} (133 meV) can be estimated from the energy difference between vertical electron transitions $S_0 \rightarrow S_1$ and $S_0 \rightarrow T_1$. This agrees approximately with the value of 725 cm^{-1} (90 meV) roughly estimated from the shift of the emission peak maxima upon cooling (see below). Hence, this Ag(I) complex represents an interesting TADF candidate.

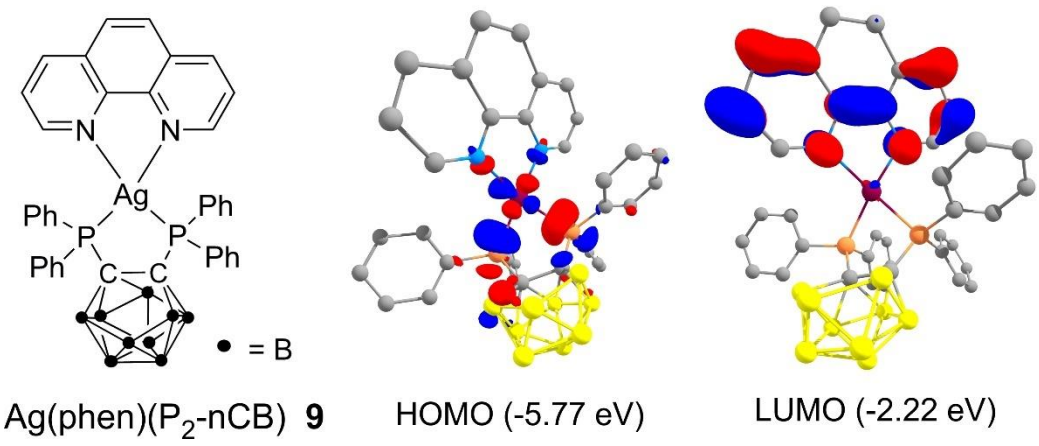

Figure 14. Chemical structure formula and calculated (M062X/def-2SVP) frontier orbital iso-surface contour plots (iso-value = 0.05) for Ag(phen)(P_2-nCB) **9**. [109] The calculations were carried out for the gas phase optimized (M06/def-2SVP) T_1 state geometry.

Figure 15 displays emission and absorption spectra of Ag(phen)(P_2-nCB) **9**. The absorption peak of low molar extinction (3020 $M^{-1} \cdot cm^{-1}$) near 400 nm is assigned to the $S_0 \rightarrow S_1$ (^{1}MLL´CT) transition, while the structures of higher allowedness and higher energy are ascribed to ligand centered transitions. (Compare also the TD-DFT results shown in the SI of Ref.[109]) The emission spectra are broad and unstructured as

usually found for charge transfer (CT) transitions. With temperature reduction from T = 300 K to 40 K, a red shift of the peak maximum of the powder material from 575 nm to 600 nm (25 nm corresponding to 725 cm^{-1} or 90 meV) is observed. Such a behavior agrees well with the occurrence of TADF. At ambient temperature, the emission stems dominantly from the singlet state S_1, while at T = 40 K, the TADF process is frozen out and only the lower energy phosphorescence from the T_1 state occurs.

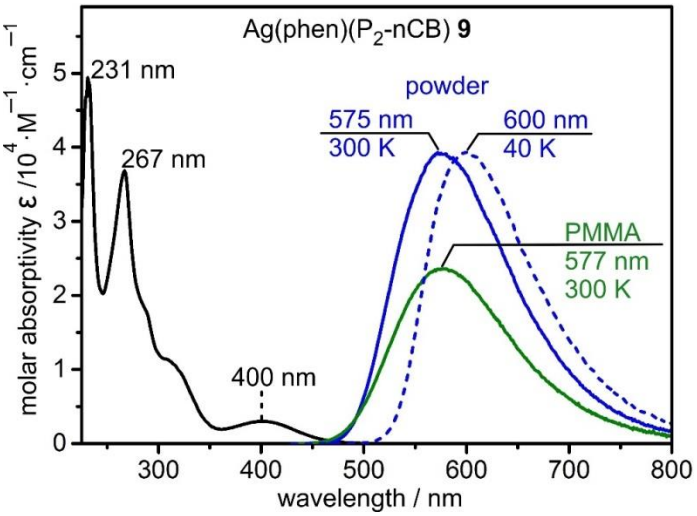

Figure 15. Emission and absorption spectra of Ag(phen)(P_2-nCB) **9** at different temperatures. The absorption spectrum is measured with a dichloromethane (DCM) solution of ≈ 10^{-5} M concentration at 300 K (black line). The emission spectra are shown in colored lines (λ_{exc} = 410 nm). The PMMA film was doped with ≈ 1 wt. % of compound **9**. [109]

For completeness, it is noted that the slight red shift of the ambient temperature emission of the PMMA-doped emitter **9**, as compared to the powder material, is related to the lower rigidity of the PMMA film given by the emitter`s environment. A corresponding behavior has already been discussed for Cu-based TADF compounds in sections 3 and 4 as well as in the literature.[31,95]

Emission quenching in Ag(phen)(P_2-nCB)

It is of particular importance for application of emitters in OLEDs that the photoluminescence quantum yield of the emitter should be as high as possible. However, for Ag(phen)(P_2-nCB), the values amount only to Φ_{PL}(powder, 300 K) = 36 %

and Φ_{PL}(PMMA doped, 300 K) = 26 % respectively.[3] (Table 6, below) Therefore, it is of interest to understand, why emission quenching is distinctly effective for this compound. For Cu(I) complexes, it is well known that flattening distortions occur upon excitation of MLCT states (section 3 and see refs. [31,115,118-119,122-123,178]). A similar behavior is also expected to be relevant for Ag(I) complexes. DFT geometry optimizations (M06/def2-SVP) show that the lowest excited (relaxed) triplet state T_1 of Ag(phen)(P_2-nCB) **9** is distinctly twisted towards planarization as compared to the ground state geometry. This distortion cannot be characterized by one simple parameter, but in a rough description, just for orientation, one may take the change of the angle $\Delta\varphi$ between two planes placed into the molecular core of the complex. (Figure 16) Related to such a distortion, the potential energy surfaces of the involved energy states are shifted with respect to each other. This leads to an increase of the Franck-Condon factors between higher lying vibrational states of the electronic ground state S_0 and the lower lying vibrational states of the excited state. The larger the Franck-Condon factors, the more efficient are non-radiative relaxation processes. [125-127] Indeed, the emission quantum yield of compound **9** with a large value of $\Delta\varphi \approx 35°$ amounts only to Φ_{PL} = 36 %, although the compound sits in a rigid crystalline (powder) environment.

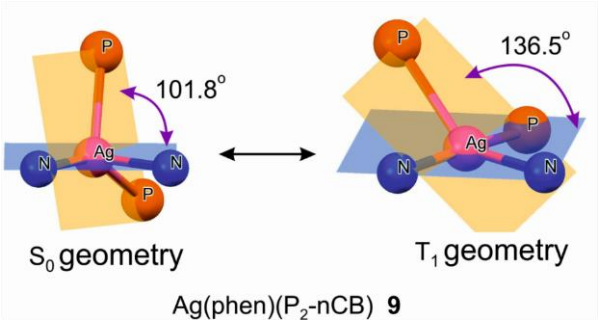

Figure 16. Schematic visualization of the geometry change between the electronic ground state S_0 and the triplet state T_1. Only the coordination core around the Ag ion is

[3] The emission quantum yield of Ag(phen)(P2-nCB) in degassed DCM solution is $\Phi_{PL} << 1$ %.

shown. The angles refer to the inclination between the P-Ag-P (orange) and N-Ag-N (blue) planes. The charge transfer excitation induces a flattening distortion characterized by a model parameter of $\Delta\varphi \approx 35°$. The calculations were carried out on the M06/def2-SVP level of theory for the gas phase conditions.[109]

These considerations lead to the suggestion to rigidify the emitter`s structure by introducing intra-molecular steric hindrances. Such an approach has already been successfully applied.[9,30-31,35,92,108-109,115,120,128] (Compare also section 3.) We will discuss this procedure in the next section applying it to Ag(R-phen)(P_2-nCB), with R representing a substitution.

Sterical hinderance. Tuning of the emission quantum yield up to 100 %

Several Ag(I) complexes comprising the P_2-nCB ligand in combination with a phenanthroline ligand, in each case differently substituted at the positions 2 and 9, are displayed in Table 6. The photophysical investigations show that with more bulky substituents on the phenanthroline ligand, the non-radiative decay rate decreases and hence, the photoluminescence quantum yield increases. For example, an increase from Φ_{PL} = 36 % found for Ag(phen)(P_2-nCB) **9** with an unsubstituted phen ligand to Φ_{PL} = 100 % for Ag(dbp)(P_2-nCB) **13** with the 2,9-di-n-butyl phenanthroline ligand is observed.[108-109] The calculated model parameter $\Delta\varphi$, describing coarsely the flattening angle, correlates with this photophysical behavior, as was expected. Without sterical hinderance, the $\Delta\varphi$ parameter amounts to ≈ 35°, while for the compounds with sterical hinderance the angle change is about three times smaller. For Ag(dbp)(P_2-nCB) **13**, for example, the $\Delta\varphi$ parameter amounts only to ≈ 12°. (Compare figures 16 and 17.) According to the significantly lower geometry change upon CT excitation, the emission quantum yield increases drastically. (Table 6)

Table 6. Photophysical data that govern TADF properties of a series of Ag(I) complexes.[108-109]

	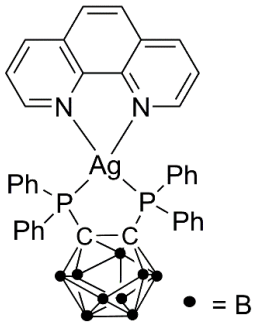	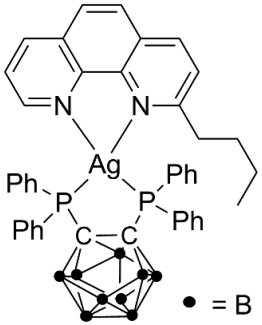	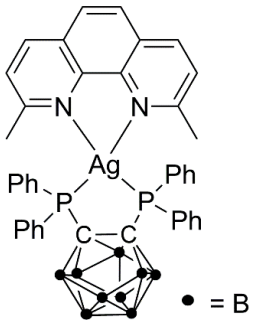	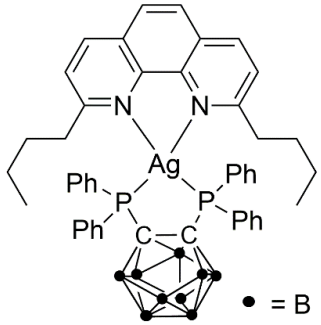
	Ag(phen)(P_2-nCB) 9	**Ag(mbp)(P_2-nCB) 10**	**Ag(dmp)(P_2-nCB) 11**	**Ag(dbp)(P_2-nCB) 13**
Φ_{PL} (300 K)	36 %	70 %	78 %	100 %
$f(S_1 \rightarrow S_0)^a$	0.0258	0.0478	0.0423	0.0536
$k^r(S_1 \rightarrow S_0)^b$	–	$2.2 \cdot 10^7$ s^{-1}	$2.2 \cdot 10^7$ s^{-1}	$5.6 \cdot 10^7$ s^{-1}
τ^r(TADF, 300 K)^c	5.3 µs	2.9 µs	3.2 µs	1.4 µs
$\Delta E(S_1-T_1)^d$	–	640 cm^{-1}	650 cm^{-1}	650 cm^{-1}
λ_{max} (300 K)	575 nm	535 nm	537 nm	526 nm

[a]TD-DFT calculated (M062X/def2-SVP) oscillator strength based on gas phase optimized (M06/def2-SVP) T_1 state geometries.
[b]Radiative decay rate of the prompt fluorescence determined from th fit of eq. (1) to experimental decay times at various temperatures.
[c]Radiative decay time measured at 300 K, essentially representing TADF.
[d]Energy gap between the lowest excited singlet and triplet states as determined from the fit of eq. (1) to experimental decay times over a temperature range of $30 \leq T \leq 300$ K.

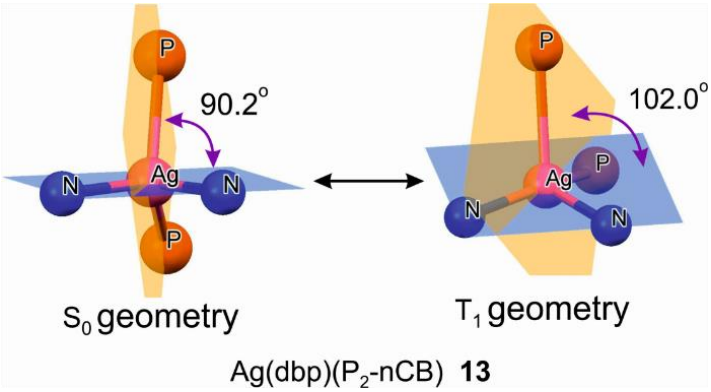

Figure 17. Schematic visualization of the geometry change between the electronic ground state S_0 and the triplet state T_1. Only the coordination core around Ag is shown. The angles refer to the inclination between the P-Ag-P (orange) and N-Ag-N (blue) planes. The charge transfer excitation induces a flattening distortion characterized by a model parameter $\Delta\varphi \approx 12°$. The geometry optimizations were carried out for gas phase conditions at the M06/def2-SVP level of theory. (Compare Figure 16) Adapted from Ref.[109]

The TD-DFT calculations (M062X/def2-SVP) carried out for the optimized T_1 state geometry reveal another important variation in the series of complexes shown in Table 6. The oscillator strength $f(S_0 \rightarrow S_1)$ of the $S_1 \rightarrow S_0$ electronic transition increases from f = 0.0258 for Ag(phen)(P_2-nCB) **9** to f = 0.0536 for Ag(dbp)(P_2-nCB) **13**, i.e. by a factor of more than two.[109] At the first sight, the reason for this increase is not obvious. However, in a computational model, as presented in Ref.[109], it can be shown that TD-DFT calculations carried out for Ag(phen)(P_2-nCB) **9**, fixed to the T_1 state geometry of Ag(dbp)(P_2-nCB) **13**, gives the $S_0 \rightarrow S_1$ oscillator strength of f = 0.0687. This value is even higher than the value, calculated for compound Ag(dbp)(P_2-nCB) **13** itself. Obviously, the effect of the complex's geometry on the $S_1 \rightarrow S_0$ oscillator strength is superior to the electronic influence of the substituents on positions 2 and 9 of the 1,10-phenanthroline ligand.[109]

The increase of the calculated oscillator strength of the series of Ag(I) complexes should also be displayed in the experimentally determined radiative rate (that is proportional to the oscillator strength). Indeed, the radiative rates $k^r(S_1 \rightarrow S_0)$ (Table 6)

show a similar increase as is seen, for example, when Ag(mbp)(P_2-nCB) with $k^r(S_1\text{-}S_0)$ = $2.2\cdot10^7$ s^{-1} is compared to Ag(dbp)(P_2-nCB) with $k^r(S_1\text{-}S_0)$ = $5.6\cdot10^7$ s^{-1}.

In summary, the drastic increase of the emission quantum yield in the series of Ag(I) complexes arranged in Table 6 is induced by two different effects. (i) Increasing sterical hindrance strongly reduces non-radiative relaxation. (ii) In parallel, the 2,9-substitutions stabilize a complex' geometry which leads to a high radiative rate. Both effects are responsible in a very favorite way for attaining the high emission quantum yield of Φ_{PL} = 100 % for Ag(dpb)(P_2-nCB).

For completeness, we also calculated the $S_0 \rightarrow S_1$ oscillator strengths for Cu(I) complexes with the same ligands. For example, TD-DFT calculation (M062X/def2-SVP) carried out for compound Cu(dbp)(P_2-nCB) in gas phase for the T_1 state geometry (M06/def2-SVP) gives an the oscillator strength value of f = 0.0660, while the value for the corresponding Ag(dbp)(P_2-nCB) complex amounts to f = 0.0536. Obviously, the change of allowedness effected by replacement of Ag(I) through Cu(I) is not very distinct.[4]

Guided by this result, it seems to be justified to relate properties based on oscillator strengths of the $S_1 \leftrightarrow S_0$ transitions of Ag(I) complexes to trends that are observed for Cu(I) complexes. In particular, comparison to the relation between the energy splitting $\Delta E(S_1\text{-}T_1)$ and the radiative rate $k^r(S_1\text{-}S_0)$, as displayed in Figure 12 (Section 5) for Cu(I) complexes, elucidates an interesting result. Inserting the data found for Ag(dbp)(P_2-nCB) with $\Delta E(S_1\text{-}T_1)$ = 650 cm^{-1} and $k^r(S_1\text{-}S_0)$ = $5.6\cdot10^7$ s^{-1} (Table 6), it becomes obvious that these data do not fit. The rate of the Ag(I) complex is about one order of magnitude higher than expected from the relation shown in Figure 12. This result is highly interesting, since it indicates, how to develop new materials that break

[4] The emission quantum yield of Cu(dbp)(P_2-nCB) powder is relatively low (Φ_{PL} = 16 %). Therefore, this material is not suitable for OLED applications.

the restrictions imposed by the simple quantum mechanical model presented in section 5. Apparently, the singlet state S_1 wavefunction of the discussed Ag(I) complexes are not simply given by the HOMO-LUMO excitation, but are distinctly modified by configurational interaction. This means, higher lying singlet states, resulting from other configurations, mix and thus, induce significantly larger $S_1 \rightarrow S_0$ transition rates. Further quantum mechanical investigations have to be carried out in this respect. Nevertheless, these results represent a guideline for the development of materials with shorter TADF decay time, as it has already been demonstrated for Ag(dbp)(P_2-nCB) **13**.[108]

Detailed characterization of Ag(dbp)(P_2-nCB)

The TADF properties of Ag(dbp)(P_2-nCB) **13** are highly attractive due to its photoluminescence quantum yield of Φ_{PL} = 100 % and the very short decay time of τ(TADF) = 1.4 µs. Therefore, in this section, we will focus on a detailed characterization of the compound`s emission properties.

The lowest excited singlet S_1 and triplet T_1 states predominantly originate from the HOMO→LUMO transition (92 %), slightly less than found for Ag(phen)(P_2-nCB) **9**. The HOMO is mainly composed of silver (13 %) and phosphorus (47 %) orbitals, while the LUMO represents a π^* orbital of the dbp ligand. (Figure 18) Thus, we can assign the two lowest excited states as ^{1,3}(MLL´CT) states with L and L´ representing P_2-nCB and dbp, respectively. According to the TDDFT calculations carried out for the optimized T_1 state geometry of Ag(dbp)(P_2-nCB) **13**, the energy separation $\Delta E(S_1\text{-}T_1)$ can be estimated to be 0.15 eV (≈ 1200 cm^{-1}). This represents an upper bound that is obtained from vertical excitations of $S_0 \rightarrow S_1$ and $S_0 \rightarrow T_1$ transitions, respectively. The calculated value is largely in agreement with the experimentally determined activation energy of $\Delta E(S_1\text{-}T_1)$ = 650 cm^{-1} (See below).

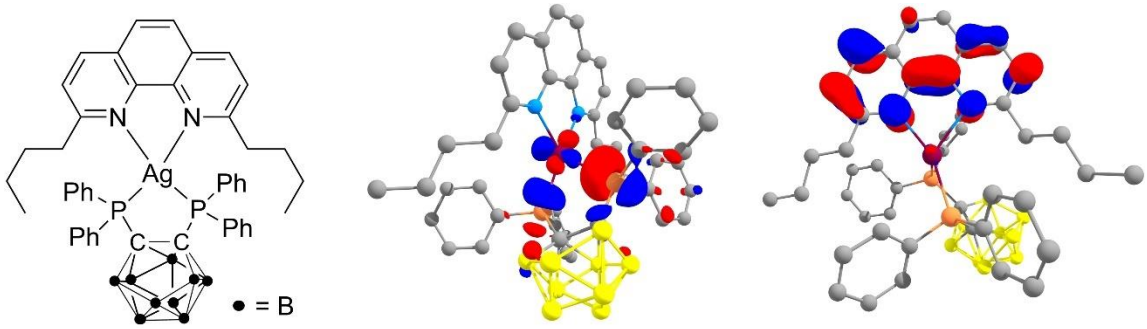

Ag(dbp)(P_2-nCB) **13** HOMO (-6.09 eV) LUMO (-2.09 eV)

Figure 18. Chemical structure formula and calculated (M062X/def2-SVP) iso-surface contour plots (iso-value = 0.05) of the frontier orbitals of Ag(dbp)(P_2-nCB) **13**. [108] The calculations were carried out for the gas phase optimized (M06/def2-SVP) T_1 state geometry.

The *n*-butyl substitutions at the 2,9-positions of the phen-ligand lead to a distinct sterical hinderance with respect to a geometry change upon the CT excitation. DFT computations show that this flattening distortion is much less expressed than found for Ag(phen)(P_2-nCB). (Compare Figures 16 and 17) As a consequence, it is expected that the emission quantum yield of the more rigid complex Ag(dbp)(P_2-nCB) **13** is higher than that of Ag(phen)(P_2-nCB), as already discussed above and as experimentally found.[5]

[5] The molecular rigidity of Ag(dbp)(P_2-nCB) is largely maintained, even if the complex is doped in PMMA, in contrast to most other TADF compounds (compare section 3 and Ref.[95]) For Ag(dbp)(P_2-nCB) doped in PMMA, Φ_{PL} drops from 100 % (powder) only to 85 %. (Table 7)

Table 7. Emission data for Ag(I) complexes as powder materials and doped in PMMA measured at different temperatures

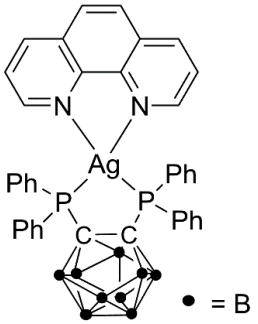

Ag(phen)(P_2-nCB) 9

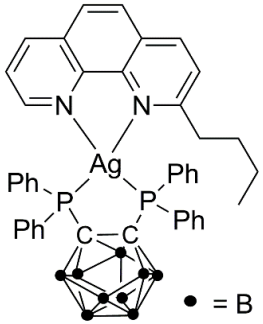

Ag(mbp)(P_2-nCB) 10

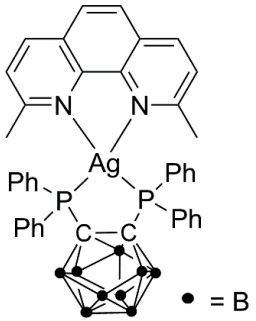

Ag(dmp)(P_2-nCB) 11

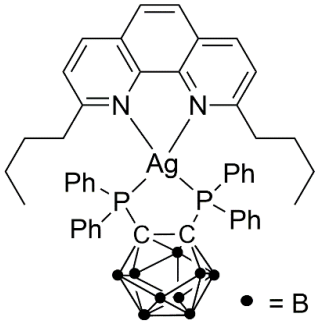

Ag(dbp)(P_2-nCB) 13

	powder	**PMMA**	**powder**	**PMMA**	**powder**	**PMMA**	**powder**	**PMMA**
λ_{max} (300 K)	575 nm	577 nm	535 nm	555 nm	537 nm	540 nm	526 nm	535 nm
Φ_{PL} (300 K)	36 %	26 %	70 %	58 %	78 %	75 %	100 %	85 %
τ(300 K)	2.0 µs		2.0 µs		2.8 µs		1.4 µs	
k^r(300 K)	$1.8\cdot10^5$ s^{-1}		$3.5\cdot10^5$ s^{-1}		$2.8\cdot10^5$ s^{-1}		$7.1\cdot10^5$ s^{-1}	
k^{nr}(300 K)	$3.2\cdot10^5$ s^{-1}		$1.5\cdot10^5$ s^{-1}		$0.79\cdot10^5$ s^{-1}		< $0.21\cdot10^5$ s^{-1} [b]	
Φ_{PL} (77 K)	15 %		70 %		68 %		87 %	
τ(77 K)	270 µs		1390 µs		804 µs		1300 µs	
k^r(77 K)	$5.6\cdot10^2$ s^{-1}		$5\cdot10^2$ s^{-1}		$8.5\cdot10^2$ s^{-1}		$6.7\cdot10^2$ s^{-1}	
k^{nr}(77 K)	$3.1\cdot10^3$ s^{-1}		$2.2\cdot10^2$ s^{-1}		$3.9\cdot10^2$ s^{-1}		$1\cdot10^2$ s^{-1}	
$\tau(T_1, 40\ K)$			1600 µs		885 µs		1570 µs	
$k^r(S_1\rightarrow S_0)$[a]			$2.2\cdot10^7$ s^{-1}		$2.8\cdot10^7$ s^{-1}		$5.6\cdot10^7$ s^{-1}	
$\Delta E(S_1-T_1)$[a]			640 cm^{-1}		650 cm^{-1}		650 cm^{-1}	

[a] determined from the fit of experimental luminescence decay times according to eq. 1, measured for a powder sample at different temperatures. [b] determined assuming 3% error for the measured Φ_{PL} value, which would allow Φ_{PL} = 97 %.

Figure 19 displays the emission spectra of Ag(dbp)(P_2-nCB) **13**. The spectra are broad and unstructured as expected for CT transitions. Even cooling to T = 1.5 K does not lead to any better resolution (not shown). However, application of methods based on the temperature dependence of the emission decay time reveals additional information, as will be demonstrated below. For the powder material, a blue shift is observed with temperature increase from T = 40 K (T_1 emission) to T = 300 K (S_1 emission) of $\Delta\lambda$ = 14 nm corresponding to 490 cm^{-1} (60 meV). This value fits approximately to the activation energy of $\Delta E(S_1\text{-}T_1)$ = 650 cm^{-1} (80 meV) as determined below. However, it is noted that the emission spectra represent transitions between Franck-Condon states, and therefore the shift of emission spectra is not very reliable to assess the $\Delta E(S_1\text{-}T_1)$ gap, especially when the excited states are of CT character.

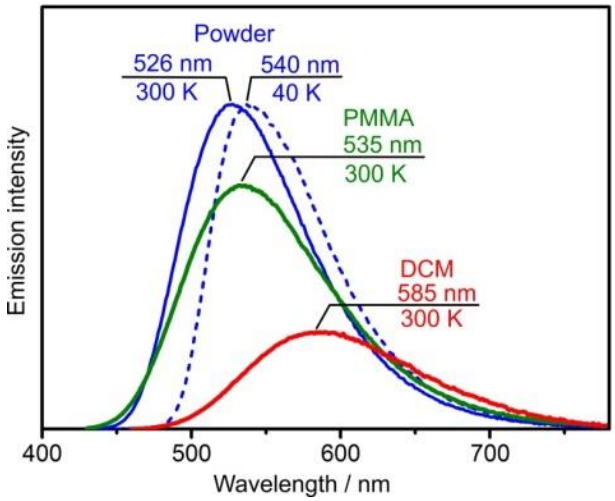

Figure 19. Emission spectra of Ag(dbp)(P_2-nCB) **13**. The measurements were carried out under different conditions, as marked in the diagram. Concentrations: PMMA: c ≈ 1 wt. %, dissolved in dichloromethane (DCM): c ≈ 10^{-5} M. λ_{exc} = 410 nm. Compare Ref.[108]

Detailed information on the electronic structure and the relevant decay processes can be obtained from time-resolving measurements, as already shown in previous sections. Figure 20a shows almost mono-exponential emission decay curves measured at

different temperatures. In Figure 20b, the decay times are plotted versus temperature. In the temperature range of 20 K ≤ T 60 ≤ K, a constant value of 1570 µs is observed (plateau). With this value and the low-temperature emission quantum yield of Φ_{PL} (77 K) = 87 % (Table 7), one can determine the radiative rate to k^r(40 K) = $5.5 \cdot 10^2$ s^{-1} (applying eq. (3), whereby it is assumed that the quantum yield at T = 40 K is the same as the measured one at T = 77 K). With temperature increase to T = 300 K, the decay time decreases drastically to τ(300 K) = 1.4 µs (at Φ_{PL} = 100 %). Accordingly, the radiative rate increases by a factor of about 1300 to k^r(300 K) = $7.1 \cdot 10^5$ s^{-1}. Obviously, such a change has to be related to the involvement of different electronic transitions at low and high temperature, respectively. At low temperature, the emission is a phosphorescence from the T_1 state and at ambient temperature it represents TADF from the S_1 state.

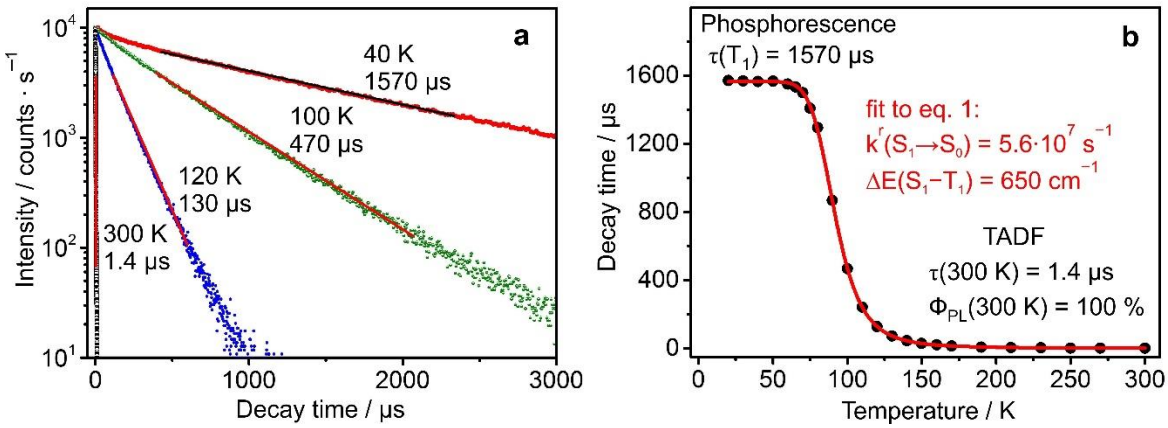

Figure 20. (a) Luminescence decay curves of Ag(dbp)(P_2-nCB) **13** powder measured at different temperatures. **(b)** Luminescence decay time (τ) plotted versus temperature. The values of k($S_1 \rightarrow S_0$) = $5.6 \cdot 10^7$ s^{-1} (18 ns) and $\Delta E(S_1\text{-}T_1)$ = 650 cm^{-1} result from a fit of eq. (1) to the experimental τ(T) data, with τ(T_1) fixed to 1570 µs as determined directly for T < 60 K (plateau). λ_{exc} = 378 nm, diode laser PB-375L, pulse width = 100 ps. Adapted with permission from [108]. Copyright © 2017, American Chemical Society.

The mono-exponentiality of the decay curves indicates fast thermalization between the involved energy states due to fast up- and down-ISC and small inhomogeneities (small

variations of $\Delta E(S_1\text{-}T_1)$) of the compounds in the powder material. In this situation, the emission decay time $\tau(T)$ of a molecular system of two excited energy states, T_1 and S_1, can be expressed by eq. (1). The fit of this equation to the experimental data (Figure 20b) gives the activation energy of $\Delta E(S_1\text{-}T_1)$ = 650 cm^{-1} (80 meV) and the radiative rate of the prompt fluorescence of $k^r(S_1 \rightarrow S_0) = 5.6 \cdot 10^7\ s^{-1}$. Formally, this value corresponds to a fluorescence decay time of $\tau(S_1)$ = 18 ns. However, the related prompt fluorescence is not directly observed, since the processes of ISC from S_1 to T_1 are about three orders of magnitude faster (Compare Ref. [119,122,134]).[135]

The experimental value of $k(S_1\text{-}S_0) = 5.6 \cdot 10^7\ s^{-1}$ found for the prompt fluorescence rate is remarkably large. Cu(I) complexes investigated so far (and that have comparable $\Delta E(S_1\text{-}T_1)$ splittings) exhibits only rates that are one order of magnitude smaller.[31] (See section 5, Figure 12) Thus, the high (prompt) fluorescence rate can be identified as a key feature that leads to the exceptionally fast TADF decay time of Ag(dbp)(P_2-nCB). This behavior fits perfectly to the large oscillator strength that is calculated for the $S_1 \rightarrow S_0$ transition. (Compare the discussion presented above in this section.)

Photophysical data for Ag(dbp)(P_2-nCB) **13** are summarized in Table 7 and in an energy level diagram shown in Figure 21. Herein, the material`s properties are highlighted: At low temperature (T < 60 K), one observes only long-living phosphorescence as the $T_1 \rightarrow S_0$ transition decays with τ = 1570 µs. Such a long phosphorescence decay time is not unusual for Ag(I) or Cu(I) compounds. [31,33,96,107,179] It displays the spin-forbiddenness of this transition. The reason is that SOC to singlet states is weak. According to the discussion presented in Refs [108-109] the next higher lying singlet state (S_4) that exhibits a different 4d orbital character than the T_1 state and that can induce SOC (following general quantum mechanical rules)[70-77] is energetically

far ($\Delta E(S_4\text{-}T_1)$ = 1.57 eV). Therefore, the singlet character mixed into the T_1 state is very small. As already mentioned in section 4, SOC via the S_1 state can be neglected.

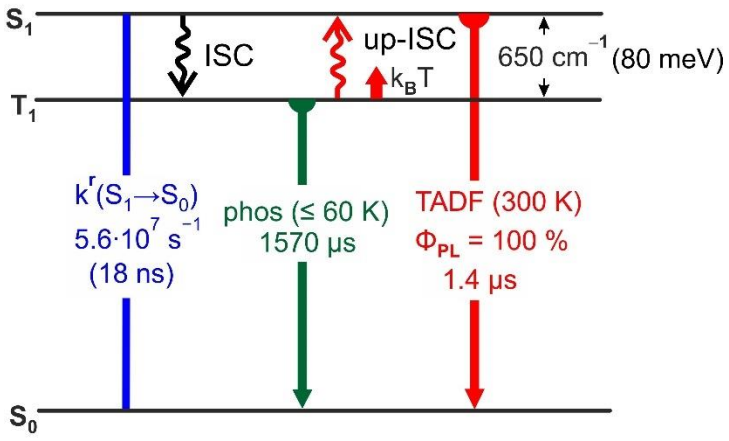

Figure 21. Energy level diagram and decay times/rates for Ag(dbp)(P_2-nCB) **13** powder. Frequently, up-ISC is also denoted as reverse ISC (RISC). Adapted from Ref. [108].

With temperature increase, the S_1 state is populated according to the thermal energy k_BT. As a consequence, the decay time decreases and a spectral blue shift is observed. This represents the TADF effect. The corresponding activation energy, as determined from the decay time plot (Figure 20b), amounts to $\Delta E(S_1\text{-}T_1)$ = 650 cm^{-1}. This energy separation is not very small (compare compound **2**, section 4), but the $S_1 \rightarrow S_0$ transition rate is much higher than for any other organometallic TADF material (with comparable $\Delta E(S_1\text{-}T_1)$ values). Thus, the TADF decay time drops to the record value of τ(TADF, 300 K) = 1.4 µs. Moreover, the Ag(I) complex represents the first TADF material with a radiative decay time comparable to those of Ir(III) complexes[1,69-70,86,89] that have become famous for OLED applications.

This short TADF decay time or the related very large radiative decay rate of k^r(TADF, 300 K) = $7.1 \cdot 10^5$ s^{-1} are responsible for the high quantum yield of Φ_{PL} = 100 %,

measured at T = 300 K. For completeness, it is mentioned that the quantum yield at T = 77 K amounts to only Φ_{PL} (77 K) = 87 %, since at that temperature the decay time is with τ(77 K) = 1300 µs relatively long, leading to a radiative rate of only k^r(77 K) = $6.7 \cdot 10^2$ s^{-1}. Using eq. (2), the non-radiative rate for this temperature is determined to k^{nr} = $1 \cdot 10^2$ s^{-1}. Thus at 77 K, the non-radiative process can moderately compete with the radiative process. But at ambient temperature, the TADF rate predominates by about three orders of magnitude. Hence, non-radiative processes are no longer relevant.

7 Conclusion and future perspectives

In this chapter, we study TADF material design based on photophysical properties investigated for a large number of compounds, in particular, with respect to OLED applications. Especially, we focus on photoluminescence properties and on the crucial requirement of designing materials that exhibit short emission decay times (high radiative rates), obviously at high emission quantum yields. The decay time should be as short as possible in order to minimize non-radiative quenching, saturation effects, and, in particular, chemical reactions that might occur in the excited state. Thus, short TADF decay time will help to strongly increase the OLED device lifetime. Here, we introduce important molecular or photophysical parameters and analyze their impact on the TADF decay time. For example, it is well known that the energy separation $\Delta E(S_1\text{-}T_1)$ between the lowest excited singlet state S_1 and triplet state T_1 should be as small as possible. Accordingly, we present detailed photophysical properties of two case studies referring to materials that exhibit a large $\Delta E(S_1\text{-}T_1)$ value of 1000 cm^{-1} (120 meV) and a small one of 370 cm^{-1} (46 meV), respectively. From these studies - extended by investigations of photophysical properties of many other Cu(I) TADF compounds - we can show that small $\Delta E(S_1\text{-}T_1)$ is not a sufficient requirement for short TADF decay

time. High allowedness of the transition between the emitting S_1 state and the electronic ground state S_0, expressed by the radiative rate $k^r(S_1 \rightarrow S_0)$, is also very important. This has often been disregarded. However, mostly small $\Delta E(S_1\text{-}T_1)$ is related to a small $k^r(S_1 \rightarrow S_0)$. As a consequence, a reduction of τ(TADF) to below a few µs might be problematic. This relation results from an investigation of a large number of Cu(I) complexes and basic quantum mechanical considerations. However, these studies are based on a situation, in fact a very frequent one, in which the involved states, S_1 and T_1, stem from the same HOMO-LUMO excitation. Other, higher lying singlet states from which the $S_1 \rightarrow S_0$ transition might borrow allowedness are energetically too far from the S_1 state. However, new materials can be designed for which this disadvantage is not prevailing. Very probably, the new TADF compound, Ag(dbp)(P_2-nCB), represents such an example. Indeed, we obtained a TADF record material with τ(TADF) = 1.4 µs at 100 % emission quantum yield, as discussed in section 6.

As a consequence, it is an important issue for future developments of TADF materials with even shorter decay times to focus on the different effects of (i) reducing the overlap of HOMO an LUMO, which leads to a smaller exchange interaction (small $\Delta E(S_1\text{-}T_1)$) and (ii) to provide other, energetically low lying singlet states from which the $S_1 \rightarrow S_0$ transition can borrow oscillator strength. For completeness, it is remarked that a different strategy to reduce the emission decay time can also be successful. It has been shown that an increase of SOC with respect to the T_1 state leading to an increase of the $T_1 \rightarrow S_0$ phosphorescence rate will open another radiative decay path. In this situation, the phosphorescence decay path is added to the TADF path.[145] Accordingly, the overall emission decay time is also significantly reduced.[31,97]

For completeness, it is mentioned that similar design rules (with the exception of increasing the phosphorescence decay rate) are also valid for purely organic TADF materials. Thus, recently it was possible to develop compounds that show extremely small $\Delta E(S_1\text{-}T_1)$ values of ≤ 10 cm^{-1} (≈ 1 meV) (<< k_BT at ambient temperature) and that carry sufficient $S_1 \rightarrow S_0$ allowedness to result in a decay time regime of only a few 100 ns. Interestingly, at this small energy separation, thermal activation is not a key property. All excitons that populate the triplet state (75 %) are transferred directly by intersystem crossing to the singlet state S_1 (that is populated independently by 25 %). This new mechanism of *Direct Singlet Harvesting* might be successful for next generation OLED applications.[180-182] An equivalent design strategy as developed for the organic materials could also be successful for organo-metallic TADF materials in future.

Acknowledgements

The authors thank the German Ministry of Education and Research for financial support in the scope of the cyCESH project (FKN 13N12668). R.C. thanks the European Research Council (ERC) for support in the framework of the MSCA RISE Project no. 645628. M.Z.S. thanks Professor Duncan Bruce (York) and The University of York for help with computational facilities. Moreover, we thank our cooperation partners for fruitful collaborations. This includes the research groups of Prof. Dr. Chensheng Ma (Shenzhen University, China), Prof. Dr. Wai-Ming Kwok (The Hong Kong Polytechnic University, Hong Kong), and Prof. Dr. Thomas A. Niehaus (Claude Bernard University, Lyon, France). In addition, we acknowledge the German Academic Exchange Service (DAAD) and the Bavaria California Technology Center (BaCaTec) for giving us the opportunity to establish and maintain our collaborations.

References

[1] H. Yersin, *Highly Efficient OLEDs with Phosphorescent Materials*. Wiley-VCH: Weinheim, 2008.
[2] W. Brütting, C. Adachi, *Physics of Organic Semiconductors*. Wiley-VCH: Weinheim, 2012.
[3] Y. Kim, S. Park, Y. H. Lee, J. Jung, S. Yoo, M. H. Lee, *Inorg. Chem.* **2016**, *55*, 909-917.
[4] Z. Liu, J. Qiu, F. Wei, J. Wang, X. Liu, M. G. Helander, S. Rodney, Z. Wang, Z. Bian, Z. Lu, M. E. Thompson, C. Huang, *Chem. Mater.* **2014**, *26*, 2368-2373.
[5] X. Q. Zhang, Y. M. Xie, Y. Zheng, F. Liang, B. Wang, J. Fan, L. S. Liao, *Org. Electron. phys. mater. appl.* **2016**, *32*, 120-125.
[6] J. Kim, K. H. Lee, S. J. Lee, H. W. Lee, Y. K. Kim, Y. S. Kim, S. S. Yoon, *Chem. Eur. J.* **2016**, *22*, 4036-4045.
[7] M. Y. Wong, G. J. Hedley, G. Xie, L. S. Kölln, I. D. W. Samuel, A. Pertegás, H. J. Bolink, E. Zysman-Colman, *Chem. Mater.* **2015**, *27*, 6535-6542.
[8] B. Minaev, G. Baryshnikov, H. Agren, *Phys. Chem. Chem. Phys.* **2014**, *16*, 1719-1758.
[9] H. Yersin, A. F. Rausch, R. Czerwieniec, in *Physics of Organic Semiconductors*, 2 ed. (Eds.: W. Brütting, C. Adachi), Wiley-VCH, Weinheim, **2012**, pp. 371-425.
[10] Y. Sun, N. C. Giebink, H. Kanno, B. Ma, M. E. Thompson, S. R. Forrest, *Nature* **2006**, *440*, 908-912.
[11] C. Adachi, M. A. Baldo, M. E. Thompson, S. R. Forrest, *J. Appl. Phys.* **2001**, *90*, 5048-5051.
[12] S. Lamansky, P. Djurovich, D. Murphy, F. Abdel-Razzaq, H. E. Lee, C. Adachi, P. E. Burrows, S. R. Forrest, M. E. Thompson, *J. Am. Chem. Soc.* **2001**, *123*, 4304-4312.
[13] S. Y. Kim, W. I. Jeong, C. Mayr, Y. S. Park, K. H. Kim, J. H. Lee, C. K. Moon, W. Brütting, J. J. Kim, *Adv. Func. Mater.* **2013**, *23*, 3896-3900.
[14] T. D. Schmidt, L. J. Reichardt, A. F. Rausch, S. Wehrmeister, B. J. Scholz, C. Mayr, T. Wehlus, R. M. Ciarnáin, N. Danz, T. C. G. Reusch, W. Brütting, *Appl. Phys. Lett.* **2014**, *105*, DOI: 10.1063/1061.4891680.
[15] V. Cherpak, P. Stakhira, B. Minaev, G. Baryshnikov, E. Stromylo, I. Helzhynskyy, M. Chapran, D. Volyniuk, D. Tomkuté-Lukšiené, T. Malinauskas, V. Getautis, A. Tomkeviciene, J. Simokaitiene, J. V. Grazulevicius, *J. Phys. Chem. C* **2014**, *118*, 11271-11278.
[16] K. Tuong Ly, R.-W. Chen-Cheng, H.-W. Lin, Y.-J. Shiau, S.-H. Liu, P.-T. Chou, C.-S. Tsao, Y.-C. Huang, Y. Chi, *Nat. Photon.* **2016**, 63-69.
[17] D. Ma, C. Zhang, Y. Qiu, L. Duan, *Org. Electron.: phys. mater. appl.* **2017**, *42*, 194-202.
[18] J. Zhang, X. Zhu, A. Zhong, W. Jia, F. Wu, D. Li, H. Tong, C. Wu, W. Tang, P. Zhang, L. Wang, D. Han, *Org. Electron.: phys. mater. appl.* **2017**, *42*, 153-162.
[19] A. Salehi, S. Ho, Y. Chen, C. Peng, H. Yersin, F. So, *Adv. Opt. Mater.* **2017**, *5*, DOI: 10.1002/adom.201700197.
[20] C. H. Yang, J. Beltran, V. Lemaur, J. Cornil, D. Hartmann, W. Sarfert, R. Fröhlich, C. Bizzarri, L. De Cola, *Inorg. Chem.* **2010**, *49*, 9891-9901.
[21] A. F. Henwood, E. Zysman-Colman, *Top. Curr. Chem.* **2016**, *374*, 36.
[22] A. K. Pal, D. B. Cordes, A. M. Z. Slawin, C. Momblona, E. OrtÍ, I. D. W. Samuel, H. J. Bolink, E. Zysman-Colman, *Inorg. Chem.* **2016**, *55*, 10361-10376.
[23] C. D. Ertl, H. J. Bolink, C. E. Housecroft, E. C. Constable, E. Ortí, J. M. Junquera-Hernández, M. Neuburger, N. M. Shavaleev, M. K. Nazeeruddin, D. Vonlanthen, *Eur. J. Org. Chem.* **2016**, *2016*, 2037-2047.
[24] A. F. Henwood, E. Zysman-Colman, *Chem. Commun.* **2017**, *53*, 807-826.
[25] C. D. Ertl, C. Momblona, A. Pertegás, J. M. Junquera-Hernández, M. G. La-Placa, A. Prescimone, E. Ortí, C. E. Housecroft, E. C. Constable, H. J. Bolink, *J. Am. Chem. Soc.* **2017**, *139*, 3237-3248.
[26] D. R. Martir, C. Momblona, A. Pertegás, D. B. Cordes, A. M. Z. Slawin, H. J. Bolink, E. Zysman-Colman, *ACS Appl. Mater. Interfaces* **2016**, *8*, 33907-33915.

[27] N. Armaroli, G. Accorsi, M. Holler, O. Moudam, J. F. Nierengarten, Z. Zhou, R. T. Wegh, R. Welter, *Adv. Mater.* **2006**, *18*, 1313-1316.
[28] S. Tang, L. Edman, in *Top. Curr. Chem., Vol. 374*, **2016**, pp. DOI: 10.1007/s41061-41016-40040-41064.
[29] C. M. Che, C. C. Kwok, S. W. Lai, A. F. Rausch, W. J. Finkenzeller, N. Zhu, H. Yersin, *Chem. Eur. J.* **2010**, *16*, 233-247.
[30] M. J. Leitl, D. M. Zink, A. Schinabeck, T. Baumann, D. Volz, H. Yersin, *Top. Curr. Chem.* **2016**, *374*, 25.
[31] R. Czerwieniec, M. J. Leitl, H. H. H. Homeier, H. Yersin, *Coord. Chem. Rev.* **2016**, *325*, 2-28.
[32] X. Hong, B. Wang, L. Liu, X. X. Zhong, F. B. Li, L. Wang, W. Y. Wong, H. M. Qin, Y. H. Lo, *J. Lumin.* **2016**, *180*, 64-72.
[33] M. J. Leitl, F.-R. Küchle, H. A. Mayer, L. Wesemann, H. Yersin, *J. Phys. Chem. A* **2013**, *117*, 11823-11836.
[34] M. J. Leitl, V. A. Krylova, P. I. Djurovich, M. E. Thompson, H. Yersin, *J. Am. Chem. Soc.* **2014**, *136*, 16032-16038.
[35] C. L. Linfoot, M. J. Leitl, P. Richardson, A. F. Rausch, O. Chepelin, F. J. White, H. Yersin, N. Robertson, *Inorg. Chem.* **2014**, *53*, 10854-10861.
[36] Q. Zhang, Q. Zhou, Y. Cheng, L. Wang, D. Ma, X. Jing, F. Wang, *Adv. Mater.* **2004**, *16*, 432-436.
[37] D. M. Zink, D. Volz, T. Baumann, M. Mydlak, H. Flügge, J. Friedrichs, M. Nieger, S. Bräse, *Chem. Mater.* **2013**, *25*, 4471-4486.
[38] D. Volz, D. M. Zink, T. Bocksrocker, J. Friedrichs, M. Nieger, T. Baumann, U. Lemmer, S. Bräse, *Chem. Mater.* **2013**, *25*, 3414-3426.
[39] D. Volz, T. Baumann, H. Flügge, M. Mydlak, T. Grab, M. Bachle, C. Barner-Kowollik, S. Bräse, *J. Mater. Chem.* **2012**, *22*, 20786-20790.
[40] M. Wallesch, D. Volz, D. M. Zink, U. Schepers, M. Nieger, T. Baumann, S. Bräse, *Chem. Eur. J.* **2014**, *20*, 6578-6590.
[41] D. Volz, Y. Chen, M. Wallesch, R. Liu, C. Fléchon, D. M. Zink, J. Friedrichs, H. Flügge, R. Steininger, J. Göttlicher, C. Heske, L. Weinhardt, S. Bräse, F. So, T. Baumann, *Adv. Mater.* **2015**, *27*, 2538-2543.
[42] M. Osawa, M. Hoshino, M. Hashimoto, I. Kawata, S. Igawa, M. Yashima, *Dalton Trans.* **2015**, *44*, 8369-8378.
[43] S. Igawa, M. Hashimoto, I. Kawata, M. Yashima, M. Hoshino, M. Osawa, *J. Mater. Chem. C* **2013**, *1*, 542-551.
[44] M. Hashimoto, S. Igawa, M. Yashima, I. Kawata, M. Hoshino, M. Osawa, *J. Am. Chem. Soc.* **2011**, *133*, 10348-10351.
[45] F. Wei, J. Qiu, X. Liu, J. Wang, H. Wei, Z. Wang, Z. Liu, Z. Bian, Z. Lu, Y. Zhao, C. Huang, *J. Mater. Chem.* **2014**, *2*, 6333-6341.
[46] J. C. Deaton, S. C. Switalski, D. Y. Kondakov, R. H. Young, T. D. Pawlik, D. J. Giesen, S. B. Harkins, A. J. M. Miller, S. F. Mickenberg, J. C. Peters, *J. Am. Chem. Soc.* **2010**, *132*, 9499-9508.
[47] Q. Zhang, T. Komino, S. Huang, S. Matsunami, K. Goushi, C. Adachi, *Adv. Funct. Mater.* **2012**, *22*, 2327-2336.
[48] G. Cheng, G. K.-M. So, W.-P. To, Y. Chen, C.-C. Kwok, C. Ma, X. Guan, X. Chang, W.-M. Kwok, C.-M. Che, *Chem. Sci.* **2015**, *6*, 4623-4635.
[49] Q. Zhang, X.-L. Chen, J. Chen, X.-Y. Wu, R. Yu, C.-Z. Lu, *RSC Adv.* **2015**, *5*, 34424-34431.
[50] X.-L. Chen, R. Yu, Q.-K. Zhang, L.-J. Zhou, X.-Y. Wu, Q. Zhang, C.-Z. Lu, *Chem. Mater.* **2013**, *25*, 3910-3920.
[51] H. Yersin, U. Monkowius, R. Czerwieniec, Patent DE 102010031831 A1, **2010**.
[52] H. Yersin, U. Monkowius, R. Czerwieniec, Patent WO 2012010650 A1, **2011**.

[53] S. Medina-Rodriguez, F. J. Orriach-Fernandez, C. Poole, P. Kumar, A. de la Torre-Vega, J. F. Fernandez-Sanchez, E. Baranoff, A. Fernandez-Gutierrez, *Chem. Commun.* **2015**, *51*, 11401-11404.
[54] C. S. Smith, C. W. Branham, B. J. Marquardt, K. R. Mann, *J. Am. Chem. Soc.* **2010**, *132*, 14079-14085.
[55] C. S. Smith, K. R. Mann, *J. Am. Chem. Soc.* **2012**, *134*, 8786-8789.
[56] R. Czerwieniec, M. Leitl, H. Yersin, Patent DE 102012101067 A1, Patent WO 2013117460 A2, **2013**.
[57] A. M. Prokhorov, T. Hofbeck, R. Czerwieniec, A. F. Suleymanova, D. N. Kozhevnikov, H. Yersin, *J. Am. Chem. Soc.* **2014**, *136*, 9637-9642.
[58] T. Hofbeck, Y. C. Lam, M. Kalbáč, S. Záliš, A. Vlček, H. Yersin, *Inorg. Chem.* **2016**, *55*, 2441-2449.
[59] C. S. K. Mak, D. Pentlehner, M. Stich, O. S. Wolfbeis, W. K. Chan, H. Yersin, *Chem. Mater.* **2009**, *21*, 2173-2175.
[60] M. Knorn, T. Rawner, R. Czerwieniec, O. Reiser, *ACS Catalysis* **2015**, *5*, 5186-5193.
[61] X.-J. Tang, W. R. Dolbier, *Angew. Chem. Int. Ed.* **2015**, *54*, 4246-4249.
[62] D. B. Bagal, G. Kachkovskyi, M. Knorn, T. Rawner, B. M. Bhanage, O. Reiser, *Angew. Chem. Int. Ed.* **2015**, *54*, 6999-7002.
[63] B. Wang, D. P. Shelar, X.-Z. Han, T.-T. Li, X. Guan, W. Lu, K. Liu, Y. Chen, W.-F. Fu, C.-M. Che, *Chem. Eur. J.* **2015**, *21*, 1184-1190.
[64] Q. Yang, F. Dumur, F. Morlet-Savary, J. Poly, J. Lalevée, *Macromolecules* **2015**, *48*, 1972-1980.
[65] A. Baralle, L. Fensterbank, J.-P. Goddard, C. Ollivier, *Chem. Eur. J.* **2013**, *19*, 10809-10813.
[66] S.-P. Luo, E. Mejía, A. Friedrich, A. Pazidis, H. Junge, A.-E. Surkus, R. Jackstell, S. Denurra, S. Gladiali, S. Lochbrunner, M. Beller, *Angew. Chem. Int. Ed.* **2013**, *52*, 419-423.
[67] H. Yersin, *Top. Curr. Chem.* **2004**, *241*, 1-26.
[68] W. Helfrich, W. G. Schneider, *J. Chem. Phys.* **1966**, *44*, 2902-2909.
[69] H. Yersin, W. J. Finkenzeller, in *Highly Efficient OLEDs with Phosphorescent Materials* (Ed.: H. Yersin), Wiley-VCH, Weinheim, **2008**, pp. 1-97.
[70] H. Yersin, A. F. Rausch, R. Czerwieniec, T. Hofbeck, T. Fischer, *Coord. Chem. Rev.* **2011**, *255*, 2622-2652.
[71] A. F. Rausch, H. H. H. Homeier, H. Yersin, *Top. Organomet. Chem.* **2010**, *29*, 193-235.
[72] A. F. Rausch, H. H. H. Homeier, P. I. Djurovich, M. E. Thompson, H. Yersin, *Proc. SPIE* **2007**, *6655*, DOI: 10.1117/1112.731225.
[73] T. Azumi, H. Miki, in *Electronic and Vibronic Spectra of Transition Metal Complexes II* (Ed.: H. Yersin), Springer Berlin Heidelberg, Berlin, Heidelberg, **1997**, pp. 1-40.
[74] H. Miki, M. Shimada, T. Azumi, J. A. Brozik, G. A. Crosby, *J. Phys. Chem.* **1993**, *97*, 11175-11179.
[75] S. Kimachi, R. Satomi, H. Miki, K. Maeda, T. Azumi, M. Onishi, *J. Phys. Chem. A* **1997**, *101*, 345-349.
[76] S. Obara, M. Itabashi, F. Okuda, S. Tamaki, Y. Tanabe, Y. Ishii, K. Nozaki, M.-A. Haga, *Inorg. Chem.* **2006**, *45*, 8907-8921.
[77] Z. Abedin-Siddique, T. Ohno, K. Nozaki, T. Tsubomura, *Inorg. Chem.* **2004**, *43*, 663-673.
[78] M. A. Baldo, D. F. O'Brien, Y. You, A. Shoustikov, S. Sibley, M. E. Thompson, S. R. Forrest, *Nature* **1998**, *395*, 151-154.
[79] M. A. Baldo, S. Lamansky, P. E. Burrows, M. E. Thompson, S. R. Forrest, *Appl. Phys. Lett.* **1999**, *75*, 4-6.
[80] Y. Kawamura, K. Goushi, J. Brooks, J. J. Brown, H. Sasabe, C. Adachi, *Appl. Phys. Lett.* **2005**, *86*, 071104.

[81] H. Sasabe, J.-I. Takamatsu, T. Motoyama, S. Watanabe, G. Wagenblast, N. Langer, O. Molt, E. Fuchs, C. Lennartz, J. Kido, *Adv. Mater.* **2010**, *22*, 5003-5007.
[82] K. Li, G. S. Ming Tong, Q. Wan, G. Cheng, W. Y. Tong, W. H. Ang, W. L. Kwong, C. M. Che, *Chem. Sci.* **2016**, *7*, 1653-1673.
[83] G. Cheng, S. C. F. Kui, W.-H. Ang, M.-Y. Ko, P.-K. Chow, C.-L. Kwong, C.-C. Kwok, C. Ma, X. Guan, K.-H. Low, S.-J. Su, C.-M. Che, *Chem. Sci.* **2014**, *5*, 4819-4830.
[84] L. F. Gildea, J. A. G. Williams, in *Organic light-emitting diodes: materials, devices and applications* (Ed.: B. A.), Woodhead Publishing, Cambridge, **2013**, pp. 77-113.
[85] E. Zysman-Colman, *Iridium (III) in optoelectronic and photonics applications*. Wiley-VCH: Weinheim, 2017.
[86] J. C. Deaton, F. N. Castellano, in *Iridium (III) in optoelectronic and photonics applications* (Ed.: E. Zysman-Colman), Wiley-VCH, Weinheim, **2017**, pp. 1-69.
[87] H. Yersin, C. Kratzer, *Coord. Chem. Rev.* **2002**, *229*, 75-93.
[88] H. Yersin, D. Donges, in *Transition Metal and Rare Earth Compounds: Excited States, Transitions, Interactions II* (Ed.: H. Yersin), Springer Berlin Heidelberg, Berlin, Heidelberg, **2001**, pp. 81-186.
[89] T. Hofbeck, H. Yersin, *Inorg. Chem.* **2010**, *49*, 9290-9299.
[90] G. J. Hedley, A. Ruseckas, I. D. W. Samuel, *Chem. Phys. Lett.* **2008**, *450*, 292-296.
[91] R. E. Daniels, S. Culham, M. Hunter, M. C. Durrant, M. R. Probert, W. Clegg, J. A. Williams, V. N. Kozhevnikov, *Dalton Trans.* **2016**, *45*, 6949-6962.
[92] R. Czerwieniec, K. Kowalski, H. Yersin, *Dalton Trans.* **2013**, *42*, 9826-9830.
[93] D. Volz, M. Wallesch, C. Flechon, M. Danz, A. Verma, J. M. Navarro, D. M. Zink, S. Bräse, T. Baumann, *Green Chem.* **2015**, *17*, 1988-2011.
[94] H. Yersin, U. Monkowius, Komplexe mit kleinen Singulett-Triplett-Energie-Abständen zur Verwendung in opto-elektronischen Bauteilen (Singulett-Harvesting-Effekt). Internal patent filing, University of Regensburg 2006. Patent DE 10 2008 033563, **2008**.
[95] R. Czerwieniec, J. Yu, H. Yersin, *Inorg. Chem.* **2011**, *50*, 8293-8301.
[96] R. Czerwieniec, H. Yersin, *Inorg. Chem.* **2015**, *54*, 4322-4327.
[97] T. Hofbeck, U. Monkowius, H. Yersin, *J. Am. Chem. Soc.* **2015**, *137*, 399-404.
[98] H. Ohara, A. Kobayashi, M. Kato, *Dalton Trans.* **2014**, *43*, 17317-17323.
[99] L. Bergmann, J. Friedrichs, M. Mydlak, T. Baumann, M. Nieger, S. Bräse, *Chem. Commun.* **2013**, *49*, 6501-6503.
[100] A. Tsuboyama, K. Kuge, M. Furugori, S. Okada, M. Hoshino, K. Ueno, *Inorg. Chem.* **2007**, *46*, 1992-2001.
[101] D. G. Cuttell, S. M. Kuang, P. E. Fanwick, D. R. McMillin, R. A. Walton, *J. Am. Chem. Soc.* **2002**, *124*, 6-7.
[102] L. Kang, J. Chen, T. Teng, X. L. Chen, R. Yu, C. Z. Lu, *Dalton Trans.* **2015**, *44*, 11649-11659.
[103] D. M. Zink, M. Bächle, T. Baumann, M. Nieger, M. Kühn, C. Wang, W. Klopper, U. Monkowius, T. Hofbeck, H. Yersin, S. Bräse, *Inorg. Chem.* **2013**, *52*, 2292-2305.
[104] J. Chen, T. Teng, L. Kang, X.-L. Chen, X.-Y. Wu, R. Yu, C.-Z. Lu, *Inorg. Chem.* **2016**, *55*, 9528-9536.
[105] X. L. Chen, R. Yu, X. Y. Wu, D. Liang, J. H. Jia, C. Z. Lu, *Chem. Commun.* **2016**, *52*, 6288-6291.
[106] M. Osawa, I. Kawata, R. Ishii, S. Igawa, M. Hashimoto, M. Hoshino, *J. Mater. Chem. C* **2013**, *1*, 4375-4383.
[107] H. Yersin, M. J. Leitl, R. Czerwieniec, *Proc. SPIE* **2014**, *9183*, DOI: 10.1117/1112.2061010.
[108] M. Z. Shafikov, A. F. Suleymanova, R. Czerwieniec, H. Yersin, *Chem. Mater.* **2017**, *29*, 1708-1715.
[109] M. Z. Shafikov, A. F. Suleymanova, R. Czerwieniec, H. Yersin, *Inorg. Chem.* **2017**, DOI: 10.1021/acs.inorgchem.1027b02002.

[110] H. Uoyama, K. Goushi, K. Shizu, H. Nomura, C. Adachi, *Nature* **2012**, *492*, 234-238.
[111] Q. Zhang, B. Li, S. Huang, H. Nomura, H. Tanaka, C. Adachi, *Nat. Photon.* **2014**, *8*, 326-332.
[112] H. Kaji, H. Suzuki, T. Fukushima, K. Shizu, K. Suzuki, S. Kubo, T. Komino, H. Oiwa, F. Suzuki, A. Wakamiya, Y. Murata, C. Adachi, *Nat. Commun.* **2015**, *6*, 8476.
[113] L.-S. Cui, H. Nomura, Y. Geng, J. U. Kim, H. Nakanotani, C. Adachi, *Angew. Chem. Int. Ed.* **2017**, *56*, 1571-1575.
[114] A. Al Mousawi, D. M. Lara, G. Noirbent, F. Dumur, J. Toufaily, T. Hamieh, T.-T. Bui, F. Goubard, B. Graff, D. Gigmes, J. P. Fouassier, J. Lalevée, *Macromolecules* **2017**, *50*, 4913-4926.
[115] D. R. McMillin, K. M. McNett, *Chem. Rev.* **1998**, *98*, 1201-1220.
[116] M. W. Mara, K. A. Fransted, L. X. Chen, *Coord. Chem. Rev.* **2015**, *282–283*, 2-18.
[117] L. X. Chen, G. Jennings, T. Liu, D. J. Gosztola, J. P. Hessler, D. V. Scaltrito, G. J. Meyer, *J. Am. Chem. Soc.* **2002**, *124*, 10861-10867.
[118] L. X. Chen, G. B. Shaw, I. Novozhilova, T. Liu, G. Jennings, K. Attenkofer, G. J. Meyer, P. Coppens, *J. Am. Chem. Soc.* **2003**, *125*, 7022-7034.
[119] M. Iwamura, H. Watanabe, K. Ishii, S. Takeuchi, T. Tahara, *J. Am. Chem. Soc.* **2011**, *133*, 7728-7736.
[120] A. Lavie-Cambot, M. Cantuel, Y. Leydet, G. Jonusauskas, D. M. Bassani, N. D. McClenaghan, *Coord. Chem. Rev.* **2008**, *252*, 2572-2584.
[121] N. Armaroli, G. Accorsi, F. Cardinali, A. Listorti, in *Photochemistry and Photophysics of Coordination Compounds I* (Eds.: V. Balzani, S. Campagna), Springer Berlin Heidelberg, Berlin, Heidelberg, **2007**, pp. 69-115.
[122] M. Iwamura, S. Takeuchi, T. Tahara, *Acc. Chem. Res.* **2015**, *48*, 782-791.
[123] S. Garakyaraghi, E. O. Danilov, C. E. McCusker, F. N. Castellano, *J. Phys. Chem. A* **2015**, *119*, 3181-3193.
[124] Z. A. Siddique, Y. Yamamoto, T. Ohno, K. Nozaki, *Inorg. Chem.* **2003**, *42*, 6366-6378.
[125] N. J. Turro, V. Ramamurthy, J. C. Scaiano, *Modern Molecular Photochemistry of Organic Molecules*, University Science Books, **2010**.
[126] W. Siebrand, *J. Chem. Phys.* **1967**, *46*, 440-447.
[127] G. W. Robinson, R. P. Frosch, *J. Chem. Phys.* **1963**, *38*, 1187-1203.
[128] C. E. McCusker, F. N. Castellano, *Inorg. Chem.* **2013**, *52*, 8114-8120.
[129] P. W. Atkins, *Quanta: A Handbook of Concepts*, Oxford University Press, **1991**.
[130] J. A. Barltrop, J. D. Coyle, *Excited states in organic chemistry*, Wiley, **1975**.
[131] A. Szabo, N. S. Ostlund, *Modern Quantum Chemistry: Introduction to Advanced Electronic Structure Theory*, Dover Publications, **1989**.
[132] C. A. Parker, C. G. Hatchard, *T. Faraday Soc.* **1961**, *57*, 1894-1904.
[133] C. A. Parker, C. G. Hatchard, *J. Phys. Chem.* **1962**, *66*, 2506-2511.
[134] L. Bergmann, G. J. Hedley, T. Baumann, S. Bräse, I. D. Samuel, *Sci. Adv.* **2016**, *2*, e1500889.
[135] C. Ma, W.-M. Kwok, R. Czerwieniec, H. Yersin, *Manuscript in Preparation*.
[136] T. Gneuss, M. J. Leitl, L. H. Finger, H. Yersin, J. Sundermeyer, *Dalton Trans.* **2015**, *44*, 20045-20055.
[137] T. Gneuss, M. J. Leitl, L. H. Finger, N. Rau, H. Yersin, J. Sundermeyer, *Dalton Trans.* **2015**, *44*, 8506-8520.
[138] H. Yersin, J. Strasser, *Coord. Chem.Rev.* **2000**, *208*, 331-364.
[139] H. Yersin, W. Humbs, J. Strasser, *Top. Curr. Chem.* **1997**, *191*, 153-249.
[140] D. S. Tinti, M. A. El-Sayed, *J. Chem. Phys.* **1971**, *54*, 2529-2549.
[141] R. W. Harrigan, G. A. Crosby, *J. Chem. Phys.* **1973**, *59*, 3468-3476.
[142] G. D. Hager, G. A. Crosby, *J. Amer. Chem. Soc.* **1975**, *97*, 7031-7037.
[143] T. Azumi, C. M. O'Donnell, S. P. McGlynn, *J. Chem. Phys.* **1966**, *45*, 2735-2742.
[144] W. J. Finkenzeller, H. Yersin, *Chem. Phys. Lett.* **2003**, *377*, 299-305.

[145] H. Yersin, M. J. Leitl, T. Hofbeck, R. Czerwieniec, U. Monkowius, Extended Singlet Harvesting for OLEDs and other electronic devices. Patent DE 102013106426 A1, Patent WO 2014202675 A1, **2013**.
[146] H. Yersin, W. Humbs, J. Strasser, *Coord. Chem. Rev.* **1997**, *159*, 325-358.
[147] R. Czerwieniec, A. M. El-Naggar, A. A. Albassam, I. V. Kityk, M. Graf, H. Yersin, *J. Mater. Sci.: Mater. Electron.* **2015**, *26*, 8394-8397.
[148] H. Yersin, R. Czerwieniec, A. Hupfer, *Proc. SPIE* **2012**, *8435*, DOI: 10.1117/1112.921372.
[149] H. Yersin, U. Monkowius, R. Czerwieniec, J. Yu, Patent DE 102008048336 A1 (2008) Patent WO 2010031485 A1 (2009), **2008, 2009**.
[150] V. A. Krylova, P. I. Djurovich, B. L. Conley, R. Haiges, M. T. Whited, T. J. Williams, M. E. Thompson, *Chem. Commun.* **2014**, *50*, 7176-7179.
[151] H. Yersin, U. Monkowius, T. Hofbeck, Patent DE 102011080240 (2013), Patent WO 2013017675 (2013), **2013**.
[152] R. Czerwieniec, H. Yersin, Patent DE 102013100181 (2013), Patent WO 2014108430 (2014), **2013, 2014**.
[153] A. D. Becke, *J. Chem. Phys.* **1993**, *98*, 1372-1377.
[154] F. Weigend, R. Ahlrichs, *Phys. Chem. Chem. Phys.* **2005**, *7*, 3297-3305.
[155] G. B. Shaw, C. D. Grant, H. Shirota, E. W. Castner, G. J. Meyer, L. X. Chen, *J. Am. Chem. Soc.* **2007**, *129*, 2147-2160.
[156] I. I. Vorontsov, T. Graber, A. Y. Kovalevsky, I. V. Novozhilova, M. Gembicky, Y.-S. Chen, P. Coppens, *J. Am. Chem. Soc.* **2009**, *131*, 6566-6573.
[157] L. Hua, M. Iwamura, S. Takeuchi, T. Tahara, *Phys. Chem. Chem. Phys.* **2015**, *17*, 2067-2077.
[158] P. A. Papanikolaou, N. V. Tkachenko, *Phys. Chem. Chem. Phys.* **2013**, *15*, 13128-13136.
[159] S. Tschierlei, M. Karnahl, N. Rockstroh, H. Junge, M. Beller, S. Lochbrunner, *ChemPhysChem* **2014**, *15*, 3709-3713.
[160] S. J. Strickler, R. A. Berg, *J. Chem. Phys.* **1962**, *37*, 814-822.
[161] J. Schmidt, H. Wiedenhofer, A. von Zelewsky, H. Yersin, *J. Phys. Chem.* **1995**, *99*, 226-229.
[162] R. Czerwieniec, W. J. Finkenzeller, T. Hofbeck, A. Starukhin, A. Wedel, H. Yersin, *Chem. Phys. Lett.* **2009**, *468*, 205-210.
[163] T. A. Niehaus, H. Yersin, *Unpublished results*.
[164] M. Wallesch, D. Volz, C. Fléchon, D. M. Zink, S. Bräse, T. Baumann, *Proc. SPIE* **2014**, *9183*, DOI: 10.1117/1112.2060499.
[165] C. Bizzarri, C. Strabler, J. Prock, B. Trettenbrein, M. Ruggenthaler, C.-H. Yang, F. Polo, A. Iordache, P. Brüggeller, L. D. Cola, *Inorg. Chem.* **2014**, *53*, 10944-10951.
[166] S. L. Murov, I. Carmichael, G. L. Hug, *Handbook of Photochemistry, Second Edition*, Taylor & Francis, **1993**.
[167] S. P. McGlynn, T. Azumi, M. Kinoshita, *Molecular spectroscopy of the triplet state*, Prentice-Hall, **1969**.
[168] M. A. El-Sayed, *J. Chem. Phys.* **1963**, *38*, 2834-2838.
[169] M. J. Leitl, Photophysical characterization of OLED relevant Cu(I) complexes exhibiting thermally activated delayed fluorescence (TADF). PhD Thesis, Universität Regesburg, **2015**.
[170] J. L. McHale, *Molecular Spectroscopy*, Prentice Hall, **1999**.
[171] T. J. Penfold, *J. Phys. Chem. C* **2015**, *119*, 13535-13544.
[172] A. Kaeser, O. Moudam, G. Accorsi, I. Séguy, J. Navarro, A. Belbakra, C. Duhayon, N. Armaroli, B. Delavaux-Nicot, J. F. Nierengarten, *Eur. J. Inorg. Chem.* **2014**, 1345-1355.
[173] C.-W. Hsu, C.-C. Lin, M.-W. Chung, Y. Chi, G.-H. Lee, P.-T. Chou, C.-H. Chang, P.-Y. Chen, *J. Am. Chem. Soc.* **2011**, *133*, 12085-12099.

[174] S. Igawa, M. Hashimoto, I. Kawata, M. Hoshino, M. Osawa, *Inorg. Chem.* **2012**, *51*, 5805-5813.
[175] C.-C. Hsu, C.-C. Lin, P.-T. Chou, C.-H. Lai, C.-W. Hsu, C.-H. Lin, Y. Chi, *J. Am. Chem. Soc.* **2012**, *134*, 7715-7724.
[176] H. Kunkely, A. Vogler, *Inorg. Chim. Acta.* **2006**, *359*, 388-390.
[177] O. Crespo, M. C. Gimeno, P. G. Jones, A. Laguna, *Dalton Trans.* **1996**, 4583-4588.
[178] G. Capano, U. Rothlisberger, I. Tavernelli, T. J. Penfold, *Journal of Physical Chemistry A* **2015**, *119*, 7026-7037.
[179] K. Matsumoto, T. Shindo, N. Mukasa, T. Tsukuda, T. Tsubomura, *Inorg. Chem.* **2010**, *49*, 805-814.
[180] H. Yersin, L. Mataranga-Popa, R. Czerwieniec, *Design of organic TADF molecules. The role of* $\Delta E(S_1\text{-}T_1)$*: From fluorescence to TADF and beyond – towards the fourth generation OLED mechanism*, 22nd International Krutyn Summer School, Krutyn, 2017 of Conference, http://www.excilight.com/node/203.
[181] H. Yersin, L. Mataranga-Popa, R. Czerwieniec, Organische Moleküle für Direktes Singulett-Harvesting mit kurzer Emissionsabklingzeit zur Verwendung in opto-elektronischen Vorrichtungen. Patent EP 17170682.3, **2017**.
[182] H. Yersin, L. Mataranga-Popa, R. Czerwieniec, Patent DE 102017101432.2, **2017**.